Modelling Voltage Response of Lithium-Ion Cells

Engineering Science Thesis

Spencer Ball

Supervised by
Professor Francis P. Dawson,
Dr. Essam Elsahwi

University of Toronto April 2023

Abstract

In this thesis, two battery models are developed and investigated for their ability to accurately simulate the terminal voltage of a lithium-ion cell with the high-level goal of improving energy management algorithms in electric vehicles. A nonlinear battery model which accounts for key electrochemical processes in the lithium-ion battery is developed and tested on experimental pulse discharge data. The interpretability and generalizability of this model are investigated, showing that the nonlinear model has the ability to provide useful insights into the charge transfer reaction. A linearized version of the nonlinear model is developed and validated using voltage responses simulated by the nonlinear model, revealing its potential to be a simpler, but still effective alternative to the nonlinear model for predicting voltage responses around specific operating points. While energy management algorithms will not likely be improved directly using the results presented in this thesis, the work established here adds to the existing literature by thoroughly documenting the battery model development and testing process such that others new to the field can learn and build upon the successes and failures of this work.

Acknowledgements

I would like to express my gratitude to Professor Francis Dawson and Dr. Essam Elsahwi for their mentorship and support throughout this research project. They have inspired me with their feedback, suggestions, and critique, which have been crucial for the development of this thesis.

I also want to thank my family and friends for their constant support and encouragement, which continues to be the unseen, ever-present driving force behind my achievements.

Introduction

The electrification of vehicle drivetrains has been a key trend in the automotive industry over the past decade [1]. The main driving force behind this trend is the promise of reduced or eliminated CO_2 emissions and other pollution during vehicle operation as compared to internal combustion engine (ICE) vehicles. Considering that the road transportation sector accounts for 16% of annual global air pollution [2], transitioning the world to electric vehicles (EVs) and thereby minimizing emissions on the road is an impactful way to minimize the effects of climate change.

One of the biggest obstacles to the mass adoption of electric vehicles (EVs) is that the average purchase price of an electric vehicle in 2022 was around $10 000 USD more than the average purchase price for a comparable internal-combustion model [2], [3]. As an EV travels more kilometers though, savings on operating costs eventually allow the total cost of ownership (purchase price and operating costs) to equal that of a comparable ICE vehicle. The specific number of kilometers it takes to reach this point of equality is termed the *break-even distance*. It is presented in [4] that once the break-even distance of EVs falls below 10 000 km, the point of early adoption is reached, where approximately 5% of all new vehicle sales are EVs. Figure 1 shows this analysis for 13 countries.

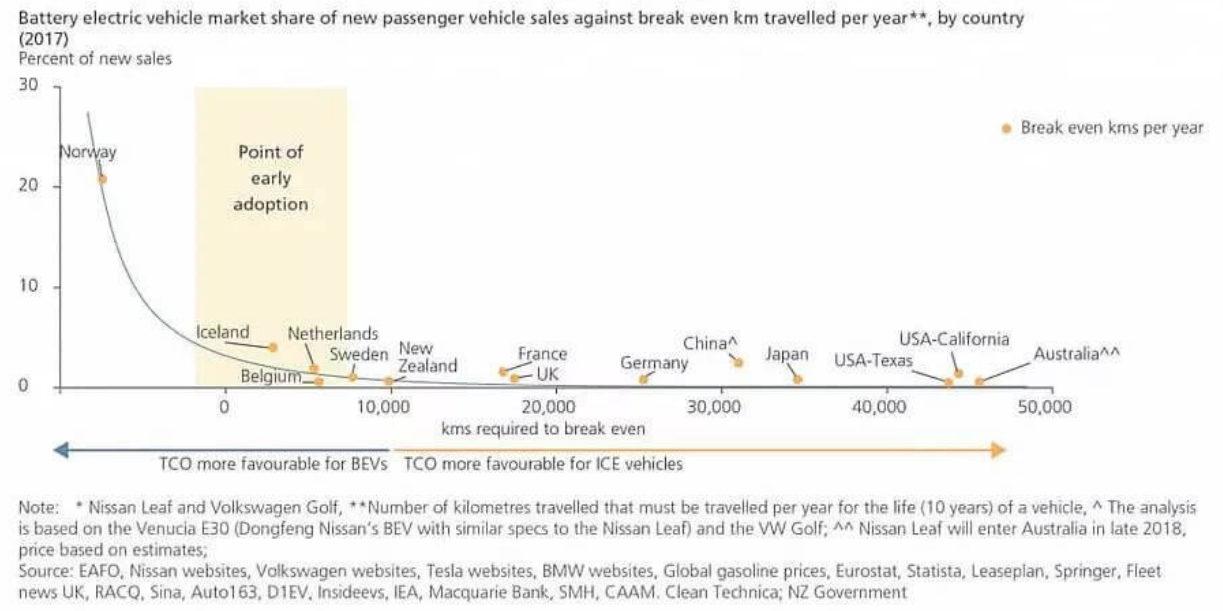

Figure 1: EV market share by break even kms from [4].

Electric vehicle operating costs are already far below ICE vehicle operating costs but their average purchase price must be reduced in order to meet this 10 000 km break-even distance. In an EV, the battery pack alone can account for up to one-third of the total vehicle manufacturing cost [5]. EV battery packs consist of hundreds to thousands of individual battery cells connected together (Appendix A). Roughly 77% of the battery pack cost is accounted for by the battery

cells alone [6]. Therefore, reducing the number of cells required to achieve the range and power requirements of a specific EV is an effective way to reduce that vehicle's purchase price.

One promising way to extract more total energy (range) and higher peak energy (power) from a given battery design is by improving the energy management algorithms used to determine the current limits imposed on battery chargers while charging and on motor controllers while discharging. These management algorithms, implemented by the battery management system (BMS) of an electric vehicle, can be designed to optimize for maximum power delivery, maximum range, or maximum battery life, and often for a balance of all three. In specific use cases, the energy management algorithms may be tailored to optimize more for one of these goals than for the others. In a race car, for example, maximum power delivery over the distance of a race could be the goal, with battery life being neglected as the battery pack could be replaced between races. In production vehicles, a balance between all three would be decided such that the vehicle maintains its range over many years, while delivering power to the motor that will satisfy the buyer. The specific design of these algorithms is outside the scope of this thesis.

This thesis is scoped around improving the quality of data which is fed into these energy management algorithms, which directly impacts their ability to accurately set charge and discharge current limits to achieve their designed performance goals. Some of the data required by these algorithms can be directly measured, such as battery voltage, current, and temperature. Other data consumed by these algorithms cannot be directly measured and must be estimated. These estimated data include state-of-charge, a measure of the amount of energy stored in a battery at a given time, state-of-health, a measure of a battery's ability to deliver its rated capacity and power compared to its original ability when new, and direct current resistance (DCR), a quantity often used by BMSs to calculate discharge current limits [7][8][9]. In this thesis, two models are developed that can be used to directly estimate the DCR of a lithium-ion battery.

A critical task for energy management algorithms is predicting the voltage drop over each cell when the pack experiences a dynamic load, such as during high acceleration, to ensure that cell voltages do not drop below their rated limits as specified by the cell manufacturer. If the energy management algorithm allows too much current to be drawn from the battery pack, one or cells in the pack may drop below their safe operating voltage, causing permanent damage to those cells, or in the worst case, a lithium fire. The DCR is typically used by the energy management algorithms to define the voltage drop of the cells in the pack under high load. If the DCR estimate is inaccurate, these algorithms must conservatively set current limits (lower than the cells could physically allow) in order to ensure that the cells in the pack with the lowest SoC stay above their minimum operating voltage when the next dynamic load happens (e.g. heavy acceleration). The models developed and investigated in this thesis attempt to predict the voltage

response of a lithium-ion battery to a given current impulse. This is equivalent to estimating the DCR.

Thesis Objectives

1. **Design and test a nonlinear battery model based partially on physical principles which can accurately reproduce terminal voltage responses to pulse discharge currents, specifically:**

    a. Understand the process of tuning a model to fit experimental data.

    b. Investigate the contributions of each component of this model to the voltage responses it generates to determine the interpretability of the model. An interpretable model is one which provides insights into the underlying physical processes that drive the system being modeled. This allows the individuals working with the model to gain a better understanding of the system, potentially enabling them to make predictions and adjust the model based on this understanding.

    c. Explore the generalizability of the model to data which it hasn't seen before. A battery model based on physical principles (even if only partially) should be capable of producing accurate voltage responses in conditions outside of those on which it was fit. A model that is generalizable is more likely to perform well in the real world where conditions are unpredictable and rarely identical to the conditions the model was developed under in the lab.

2. **Linearize the nonlinear battery model and investigate the limits of its accuracy around the operating point at which it was fit, specifically:**

    a. Starting with an artificially generated small-signal current profile that allows us to evaluate the linearized model about an operating point, use the previously validated nonlinear model to generate a voltage response in place of experimental data, and ensure the linearized model can mimic this response.

    b. Increase, in small steps, the *magnitude* of the imposed pulse discharge currents to find at what magnitude the linearized model fails to produce similar results to the nonlinear model.

    c. Increase, in small steps, the *duration* of the imposed pulse discharge currents to find at what duration the linearized model fails to produce similar results to the nonlinear model.

Document Overview

This document proceeds in the following sections.

1. **The Battery Management System:** The battery management system of an electric vehicle is described at a functional level to provide context and motivation for developing battery models which can accurately simulate the behavior of lithium-ion batteries.

2. **Challenges in Estimating Battery Behavior:** The dominating processes that drive lithium-ion battery behavior are described. The nonlinear, time-varying relationships between key parameters that dictate battery behavior are presented. This section motivates the development of battery models which both:

    - Take into account the key electrochemical processes occurring in lithium-ion batteries, so the model designer develops models grounded in reality which are both interpretable and generalizable.

    - Evolve over time to account for the changing nonlinear relationships between processes in the battery.

3. **Designing a Battery Model:** A high-level description of the battery model design process is presented along with the fundamental information needed to design a battery model. Key trade-offs that must be considered in the design process are discussed. The benefits and drawbacks of different model types are explored.

4. **A Minimal Nonlinear Circuit Model of a Lithium-Ion Cell & Results:** The chosen nonlinear battery model is presented and the experimental results are analyzed in the context of the goals of this thesis.

5. **Linearizing the Nonlinear Circuit Model & Results:** The process of linearizing the nonlinear battery model about an operating point is demonstrated. The experimental results are analyzed in the context of the goals of this thesis.

The Battery Management System

Currently, Lithium-ion battery cells are the primary choice for electrochemical energy storage in production EVs. This is due to their high energy density, enabling lighter battery packs, flat discharge curve, enabling consistent power delivery even at lower states-of-charge (SoC), and relatively low cost [10]. Lithium-ion battery packs in EVs must be paired with a battery management system (BMS) for several reasons:

- **Safety:** Lithium-ion batteries can be dangerous if managed improperly. They have a tendency to overheat and can catch fire or explode if they are overcharged, over-discharged, or operated at excessively high temperatures. A BMS directly measures each battery cell's temperature and voltage, as well as the combined current flowing into or out of the pack to provide input data to algorithms which ensure that each cell operates within safe limits as defined in the datasheet provided by the cell manufacturer.

- **Performance:** A BMS optimizes the performance of the battery by controlling the maximum rates of charging and discharging at all times. The precise meaning of performance is discussed below in 'Energy Management Algorithms'.

- **Battery Life:** A BMS helps to extend the life of the battery cells by limiting the maximum SoC while charging and the minimum SoC while discharging to avoid adverse chemical reactions which can decrease the capacity and power capability of the cells. This increases the time the cells can operate effectively before needing to be replaced, which is a costly and time-consuming process.

A BMS is composed of several hardware and software components that work together to monitor and control the battery. These components can vary depending on the requirements of a specific vehicle, but the basic components of a BMS generally include:

- **Voltage, temperature, and current sensors:** These components measure each cell's voltage and temperature individually, as well as the total current being pushed through all of the cells, as measured on the high voltage bus.

- **Balancing circuitry:** Keeps all cell voltages in the pack as close to each other as possible, as the ability of a battery pack to deliver a certain current is typically determined by the cell with the lowest voltage [11]. Voltage discrepancies between cells are usually caused by manufacturing tolerances or previous damage.

- **Control and protection circuitry:** Prevents overcharging, over-discharging, and other forms of electrical abuse by controlling current flow with components such as relays and mosfets.

- **State estimation algorithms (battery monitoring):** These algorithms make their best guess at quantities that are difficult to directly measure under load, such as the battery's remaining capacity (state-of-charge, SoC) overall health (state-of-health, SoH), and direct current resistance (DCR). The continuous determination of these battery states during operation (online) is known as ‘battery monitoring’.
    - **SoC:** A measure of the amount of energy stored in a battery at a given time, expressed as a percentage of its total capacity.
    - **SoH:** A measure of a battery's ability to deliver its rated capacity and power, expressed as a percentage of its original capabilities when new.
    - **DCR:** A quantity used to predict the cell voltage drop under load. This is defined in more detail in the ‘Challenges in Estimating Battery Behavior’ section later in this document.

- **Energy management algorithms:** These algorithms synthesize sensor measurements, SoC, SoH, and DCR estimates to try to optimize energy flowing in and out of the battery to achieve various performance goals. For each of the below optimization cases, the amount of performance gained is limited by the magnitude of error in the sensor measurements and in the SoC, SoH, and DCR estimates.
    - When optimizing for vehicle acceleration, maximizing the discharge current limit whenever possible is desirable because this allows the vehicle powertrain to use more power, enabling higher torque at the wheels. Techniques such as maximizing the allowable duration of pulse discharges higher than the nominal discharge rate of the battery cells can be used to optimize for higher peak power. The DCR is the primary input parameter used to specify the discharge current limit [7][8][9].
    - When optimizing for vehicle range, algorithms involving electrical efficiency and power loss maps can be used to find the optimum operational conditions that ensure lower power loss [12].
    - When optimizing for battery life, the BMS will try to keep the battery constantly between 80% and 20% SoC because it reduces stress on the internal materials of the cells. When a lithium-ion cell is charged to its maximum rated voltage, the cathode’s crystal structure can degrade, reducing the battery’s overall capacity over many charge-discharge cycles. Similarly, when a lithium-ion cell is discharged to its minimum rated voltage, the anode’s crystal structure can degrade, also reducing the battery’s overall capacity. A common practice in new EVs is to oversize the battery in order to build in a ‘grace capacity’ where the

battery will only be used between 80% and 20% until its capacity degrades to the point where range would be reduced. At this point, the BMS allows a higher total charge and discharge to allow the vehicle to still meet its range requirements. Eventually, the entire grace capacity is used and the vehicle range will begin fading as the battery degrades [13].

In the case of consumer road vehicles, a balance must be struck between optimizing for acceleration, range, and battery life to achieve the vehicle specifications that will sell best in the current market.

- **Communication interfaces:** These interfaces exchange data such as current limits, state-of-charge, and state-of-health with other systems and devices, such as battery chargers and motor controllers, to ensure these devices don't impose currents on the battery that would push its cells out of their rated voltage or temperature limits.

- **Microprocessor(s):** In order to process sensor data, control the balancing circuitry, execute the above-mentioned algorithms, and communicate with other devices in the vehicle, a microprocessor, or multiple microprocessors, are incorporated into the BMS. Generally, the cheapest and lowest-power processor capable of completing the above tasks is selected. Minimizing the cost of every component is key in production vehicles as small savings in the cost of each vehicle can result in enormous savings when that vehicle is mass-manufactured. Minimizing the power consumption of each component in the BMS is also important as this allows for longer battery life, especially when the vehicle is parked for extended periods of time as the control electronics in the BMS must always remain active to constantly ensure the safety of the battery.

Figure 2 shows a visual representation of the operational regions overseen by a BMS. On the X-axis is 'Open Circuit Voltage' (OCV) which is also known as the resting voltage of the battery. The OCV can be measured by disconnecting the battery from all load and waiting a sufficient period of time such that the voltage measured across the battery terminals is approximately constant. On the Y-axis is the temperature of the battery in degrees Celsius. The regions in the diagram are as follows:

- **Normal Function:** in this region, the BMS sets the highest charge and discharge current limits possible for the given battery design at optimal OCV and temperature, as specified by the manufacturer in the datasheet.

- **Reduced Current Limits:** The next region radially outwards is the region of 'reduced current limits', where the BMS begins lowering the maximum discharge and charge current limits to ensure that no load imposed on the battery is high enough to push it

outside of its rated voltage or temperature limits, as defined by the manufacturer in the datasheet. The function that describes how these limits are reduced can be grouped into the ‘Energy Management Algorithms’ component of the typical BMS described above.

- **Blocked Operation:** Moving radially outwards again, we find the region of ‘blocked operation’, where the BMS sets charge and discharge current limits to zero to prevent a predicted violation of manufacturer-specified OCV and/or temperature limits. A brief description of why each extreme can damage the cells is below.
    - **Charging at Low Temperature:** If you try to charge a lithium-ion cell below its minimum operating temperature (usually <0°C / 32°F), a chemical process known as 'lithium plating' takes place. This happens because the charging current compels the lithium ions to move faster than their typical reaction rate at the given temperature, leading them to collect on the anode surface [14]. This causes most of the lithium ions to fail to insert into the molecular lattice of the anode and instead they plate the anode with metallic lithium. This can be an irreversible process and can permanently reduce the energy storage capacity of the cell. Electric vehicles will use their battery capacity to heat cells to a temperature at which they can be charged. This is one reason why electric vehicles will struggle to ever fully replace internal combustion engines fully - In cases where people park outside for extended periods of time in cold weather their battery may completely deplete itself attempting to keep the cells warm. This leaves the user with an inoperable, unchargeable vehicle.
    - **Discharging at Low Temperature:** When discharging a lithium-ion cell at low temperatures (<0 °C), it will have reduced capacity. This decrease in capacity is caused by an increase in internal resistances - primarily, slower solid-state diffusion and charge transfer reactions. These slower reaction rates are caused by multiple factors. One factor is the molecular lattice of the electrodes contracting at lower temperatures, making it more difficult to extract lithium-ions from this lattice and insert them back in on the opposite electrode [15]. Another factor is the fact that all matter moves more slowly as temperature decreases.
    - **Charging or Discharging at High Temperature:** In the case of either charging or discharging a lithium-ion cell, the temperature of the cell will rise due to energy loss over the internal resistances of the cell. When the cell reaches a certain high-temperature threshold, the BMS will start lowering the charge and discharge current limits by multiplying them by a factor proportional to the difference between the measured cell temperature and the maximum rated cell temperature. These limits are reduced to zero when the cell temperature reaches the maximum rated temperature.

- **Discharging at Low SoC:** As a lithium-ion cell approaches its lowest rated voltage, or state-of-charge, or both, the BMS must start lowering the maximum allowable discharge rate to ensure the cell remains above its lowest rated voltage in the case that the maximum discharge current is commanded.
- **Charging at High SoC:** A common way to charge lithium-ion cells is using the 'constant-current, constant-voltage' method. In this method, a high charging current is applied from low SoC until the measured terminal voltage of the cell reaches the maximum rated voltage specified by the cell manufacturer. At this point, a constant charging voltage, equal to the maximum rated cell voltage, is applied to the cell such that the charge current gradually drops off as the cell's open-circuit voltage approaches its maximum rated terminal voltage. This drop off is caused See figure 3 below for an illustration of this charging method.

- **Critical Threshold:** This outermost layer of the diagram represents a critical failure of the BMS. When lithium-ion cells reach these extremes, they may be damaged to the point of needing immediate replacement. In the worst case, a thermal runaway event is triggered where the cells catch fire and explode. Thermal runaway is a scenario where the temperature of a lithium-ion cell increases rapidly and uncontrollably, causing the cell to release energy in the form of heat, gas, and sometimes flames. This can result in a self-sustaining and potentially catastrophic chain reaction in neighboring cells, leading to a fire or an explosion.

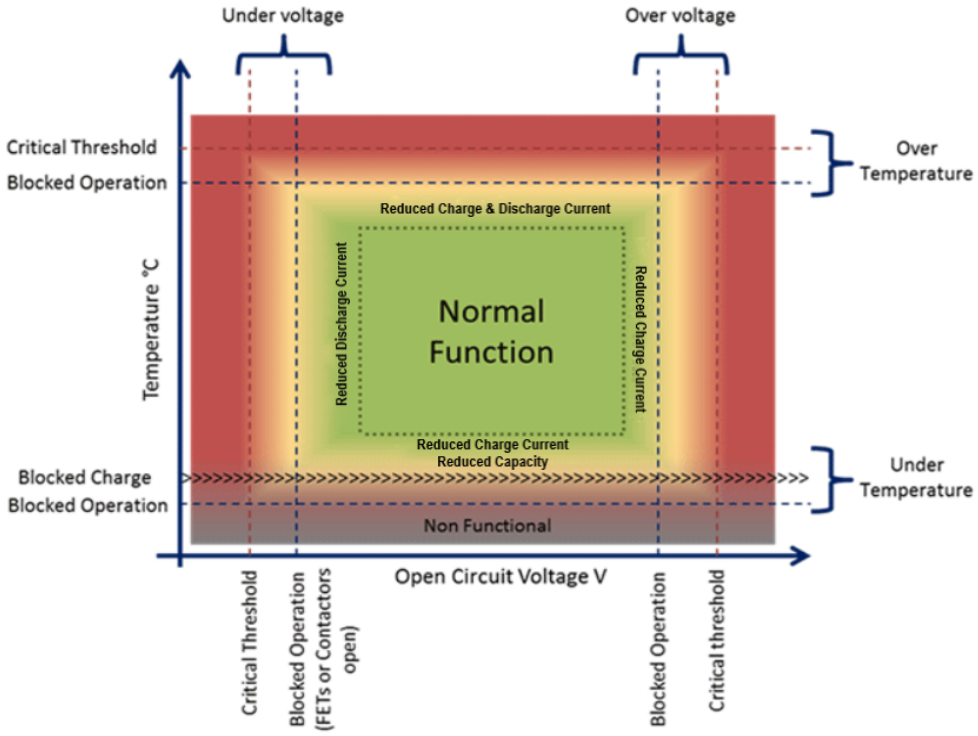

Figure 2: Operational regions of a lithium-ion battery, managed by the BMS [16].

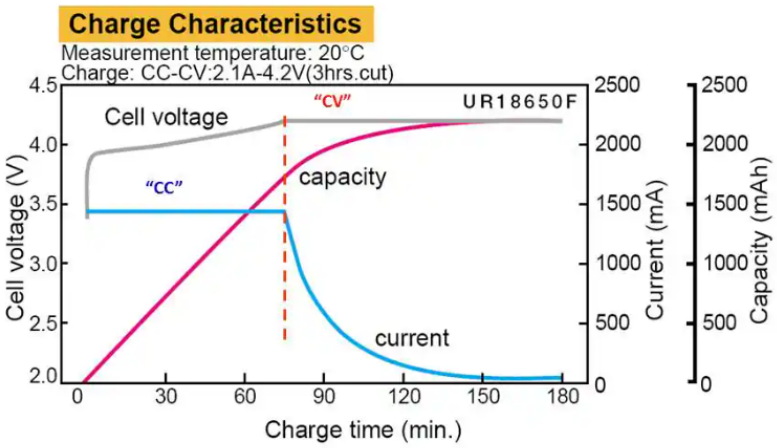

Figure 3: A typical constant-current, constant-voltage charging process [17]. The blue trace is charge current, with "CC" denoting the constant current region. The gray trace is cell voltage, as measured at the terminal, with "CV" denoting the constant voltage region. The red/pink trace is cell capacity (mAh).

Challenges in Estimating Battery Behavior

Modeling lithium-ion batteries is a challenging problem because these batteries exhibit complex electrochemical behavior that involves multiple physical and chemical processes. These processes occur at different time scales and they interact with each other in a nonlinear way. There are three dominant processes that must be considered by any model hoping to reproduce the behavior of real lithium-ion batteries.

1. **Charge Transfer Reaction:** The transfer of lithium ions between the electrode and the electrolyte during charging and discharging in lithium-ion batteries is known as the charge transfer reaction. The mathematical model used to describe this reaction is called the Butler-Volmer equation. This equation takes into consideration various factors related to the kinetics of the charge transfer reaction, such as the exchange current density, which represents the rate of the electron transfer at an electrode surface when the net current is zero. Incorporated into the exchange current density are coefficients representing the solid lithium concentrations at the surface of an electrode particle and the symmetry of the energy barrier for the reaction between the forward and reverse reactions (charging and discharging) [18]. In more detail, this symmetry is the ratio between the external energy required for the reaction to proceed in the forward direction versus the reverse direction.

2. **Conductivity of the Electrodes and the Electrolyte:** The electrodes and electrolyte in any battery have non-zero resistances that impede the migration of electrical energy across the battery. These resistances also change as the battery charges, discharges, ages, and changes temperature. Using Raman spectroscopy on $LiMn_2O_4$ spinels, a material used in the cathode of many commercial lithium-ion cells, researchers have found that the level of intercalation in the cathode of lithium-ion cells can influence the electronic conductivity of the electrode [19]. The level of intercalation in the electrodes (the amount of lithium ions embedded in the crystal lattice of the electrode material) changes as a battery charges or discharges because lithium ions are moving from one electrode to the other. Additionally, intercalation levels are reduced as a battery ages and the electrodes become damaged, reducing their ability to accept lithium ions. Furthermore, the concentration of ions in the electrolyte is known to affect the ionic conductivity in the cell [20]. The concentration of electrolyte changes during battery use for several reasons. One factor is the consumption of electrolyte during the formation of the solid electrolyte interphase (SEI) on the negative electrode [21]. This layer is formed through reactions between the electrode material and the electrolyte, blocking electron transfer into the electrolyte but allowing lithium ions through. Its formation consumes a portion of the electrolyte, thereby lowering its concentration.

3. **Solid-State Diffusion:** In lithium-ion batteries, solid-state diffusion refers to the movement of lithium ions through a solid-state electrolyte that separates the two electrodes. In most lithium-ion batteries used in electric vehicles, the electrolyte is made of a solid material that allows lithium ions to move through it while blocking the flow of electrons. One factor that can affect the rate of solid-state diffusion is temperature. As temperature decreases, the rate of diffusion decreases as well [22]. As mentioned for electrolyte conductivity, the rate of ion diffusion across the electrolyte is also reduced by the formation of the SEI. Finally, as a lithium-ion battery ages, the structure of the electrodes and electrolyte change with mechanical stress caused by the expansion and contraction of each electrode during charging and discharging, chemical degradation, and material loss. These processes alter the physical pathways through which the lithium-ions move across the battery. This can alter the solid-state diffusion rate.

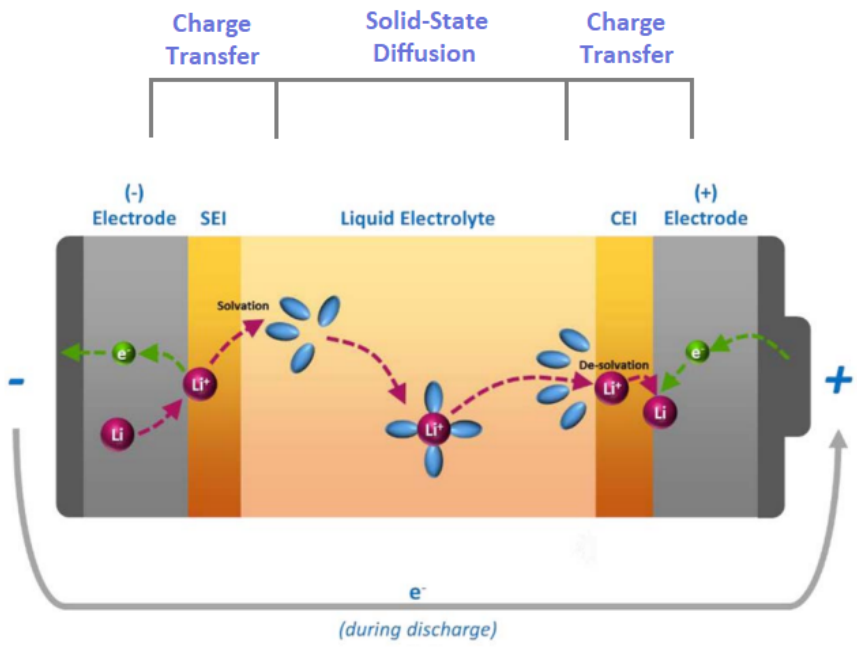

Figure 4: Key electrochemical processes in a lithium-ion battery [23].

Now that the key electrochemical processes that dominate lithium-ion battery behavior have been established, it is useful to understand how they interact with each other and change under various conditions. Defining a property known as the 'direct current resistance' (DCR) will help to illustrate these dynamics.

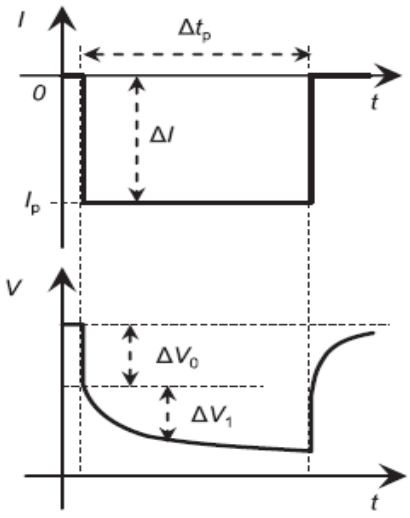

Figure 5: Pulse discharge test [7].

Figure 5 shows a typical pulse discharge test, where a lithium-ion battery at rest is subject to a stepped current and the resulting voltage response being measured across its terminals is recorded. ΔV_0 is the voltage drop caused by the combined electrical resistance of the electrodes and the ionic resistance of the electrolyte. ΔV_1 is primarily a result of the charge transfer reaction. ΔV_1 begins where the nearly instant voltage drop ΔV_0 ends (a few hundred milliseconds after the pulse discharge is applied), and ends where the approximately linear part of the response begins. The nearly linear section of the voltage response after these two drops is primarily due to the effects of solid-state diffusion. The direct current resistance is defined in the literature [7] as $(\Delta V_0 + \Delta V_1) / I_p$. This quantity is often used by battery management systems to calculate discharge current limits as its time constant is in the range of interest for power predictions (1-20 seconds) [8] [9].

Researchers have investigated how the DCR evolves under various temperatures, current rates, states-of-charge, and aging conditions [7]. The results of this investigation prove useful in understanding how the resistances of the electrodes and electrolyte as well as the charge transfer reaction are affected by conditions regularly seen in real world applications of lithium-ion batteries, including electric vehicles. The diagrams below plot 'relative resistance' against current. Relative resistance is defined here as the measured resistance divided by the resistance at a 1C current rate (40 A for investigated cell).

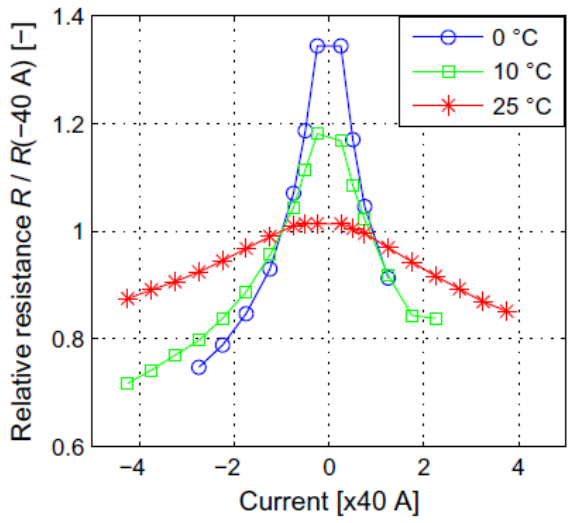

Figure 6: DCR of a new 18650 lithium-ion cell under various discharge currents and temperatures [7].

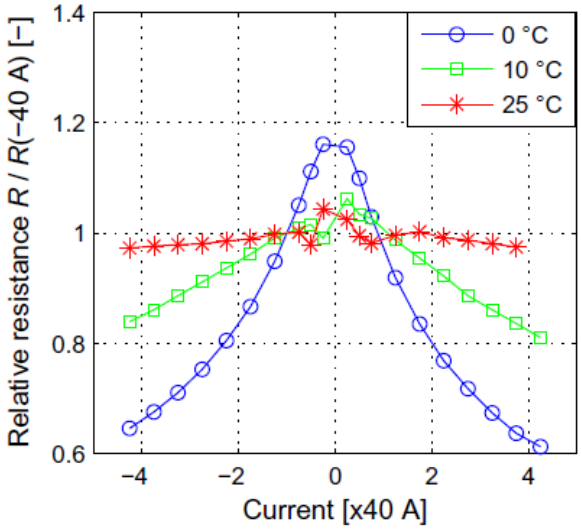

Figure 7: DCR of an aged 18650 lithium-ion cell under various discharge currents and temperatures [7].

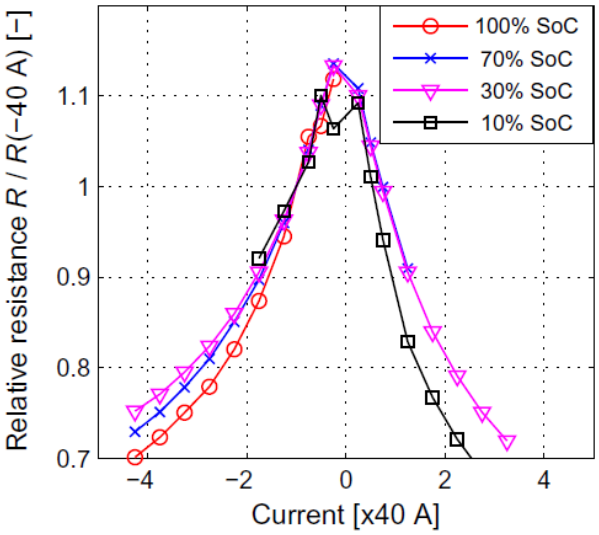

Figure 8: DCR of a new 18650 lithium-ion cell under various discharge currents and SoCs [7].

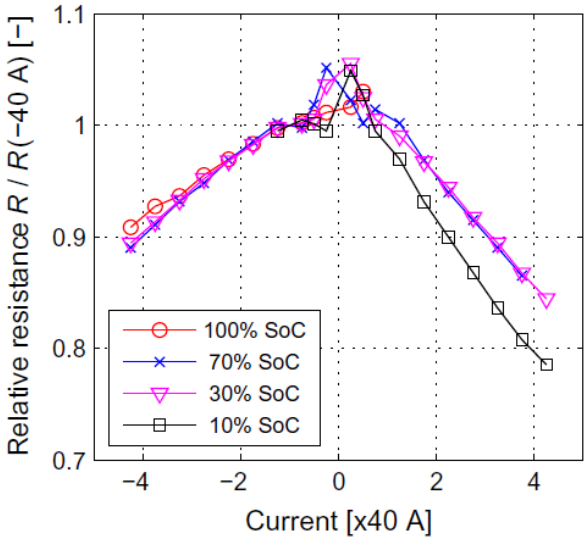

Figure 9: DCR of an aged 18650 lithium-ion cell under various discharge currents and SoCs.

It is clear from the above results that the DCR depends strongly on the discharge current applied and that this relationship is highly nonlinear and multivariate. The investigation of this relationship in [7] can be summarized as follows:

- **Effect of Temperature:** In new cells, it is found that the current dependency of the DCR is negligible at 25℃ but significant at lower temperatures. With aged cells, the dependency is notable at 25℃ and increases more significantly at lower temperatures as compared to new cells.

- **Effect of SoC:** Unlike with temperature, the current dependency of the DCR does not change substantially with SoC at a fixed temperature and aging state. Generally, the DCR increases when SoC is at the high and low ends of the allowable range. The specific SoC at which this increase happens depends on the aging state of the battery which is discussed in the next point.

- **Effect of Aging:** The basic trend is that the DCR increases over the battery's lifetime. This means that the discharge current a battery can deliver at a given temperature and state-of-charge decreases over the cell's lifetime. However, this relationship is more complex in reality and must be investigated in detail and accounted for in each given application. It is found for the cells tested in [7] that the temperature dependency of the resistance remains in its exponential form as the battery ages but is scaled by a factor depending on the aging state. In contrast, the dependency on the SoC changes significantly. In new cells, resistance increases notably above 90% SoC and below 30% SoC. In aged cells though, these regions expand to above 70% and below 50% SoC.

These results motivate the designer of BMS energy management algorithms to incorporate a model for the DCR which evolves over time to account for changing operating conditions.

Designing a Battery Model

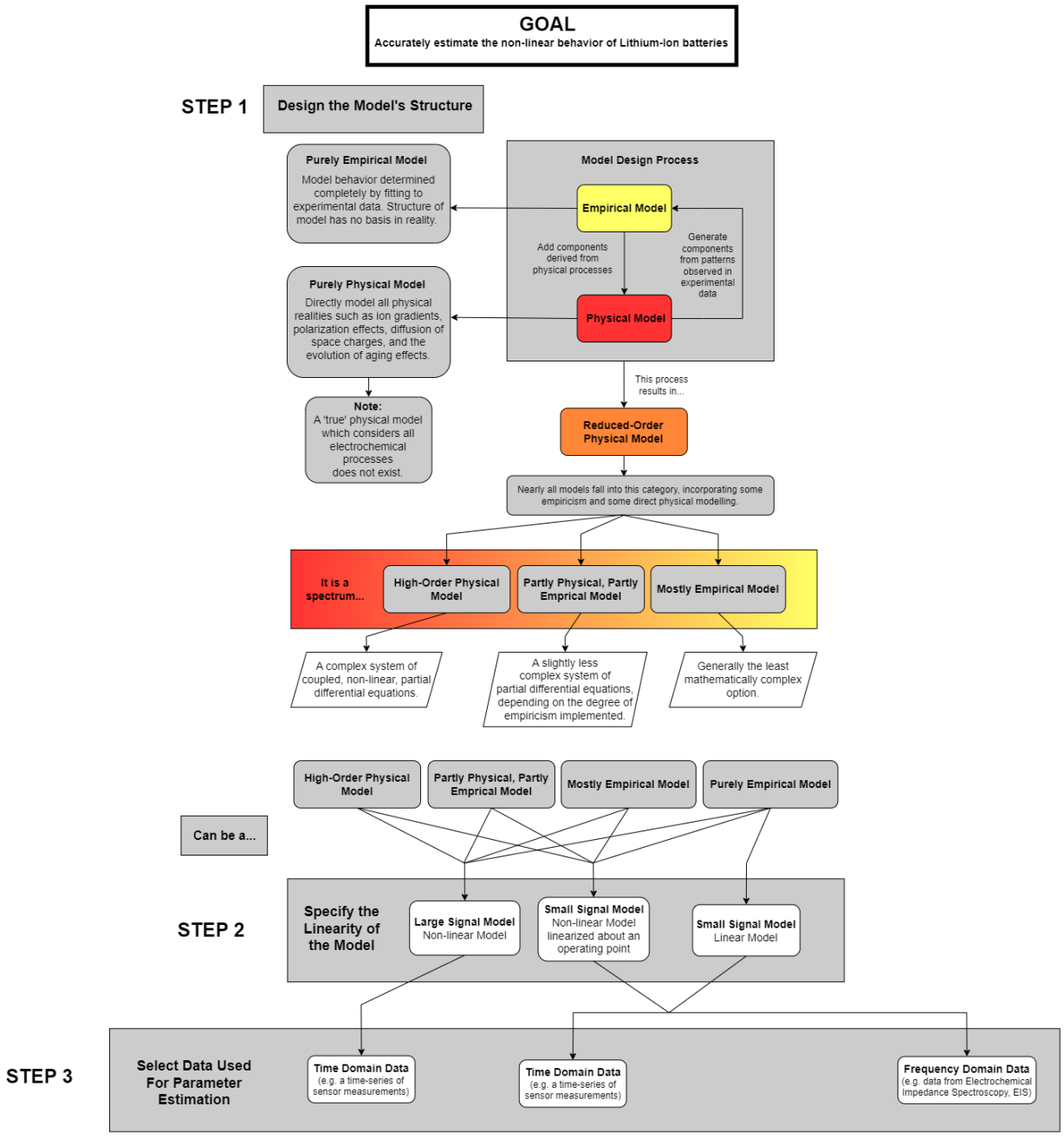

Figure 10: A general battery model design process in flow chart form.

Step 1: There are many considerations that have to be made when designing a model to accurately estimate the behavior of a lithium-ion battery. The primary trade-off to be considered is between model complexity and accuracy. The ‘Model Design Process’ block in figure 10 illustrates the process of negotiating this trade-off between complexity and accuracy. Theoretically, the model with the highest accuracy would be one which models the behavior of

each lithium ion, each molecule of the electrode and electrolyte, and all the interactions between these particles. This is shown in figure 10 as the 'Purely Physical Model', which considers every physical process happening in the lithium-ion cell. In reality, a model like this does not exist. While promising the highest accuracy, developing one of these models is impossible in reality due to the incomprehensible complexity involved. With higher model complexity comes the need for higher computational power - modeling each molecule in the battery would be infeasible with even the most powerful modern computers. Additionally, understanding the behavior of a model with such immense complexity would be nearly impossible. For example, if the model was behaving incorrectly, understanding what specifically is going wrong in order to intervene and fix the model would likely be ineffective. Despite potentially losing model accuracy by reducing the complexity of the explicitly modeled elements in the system, there is much to be gained by simplifying a model as much as possible while maintaining the accuracy necessary for a given application.

Models based on physical principles are those that are constructed based on established scientific laws and theories. In contrast, purely data-driven models are constructed based on patterns observed in data, without any prior knowledge of the underlying physical mechanisms. Some advantages of models based on physical principles over data-driven models include:

- **Interpretability:** Models based on physical principles are often more interpretable than purely data-driven models, meaning they can provide insights into the underlying physical processes that drive the system being modeled. This means the behavior of the model is more likely to be understood by researchers who already understand the field of electrochemistry. This allows researchers to gain a better understanding of the system, and to make predictions and develop interventions based on this understanding.

- **Better generalizability:** The universality of physical principles means that they apply in a wide range of operating conditions. This means that models based on physical principles are often more generalizable than purely data-driven models, which may only be valid in the specific context in which they were trained, unless extensive testing outside of that training data says otherwise.

- **Data efficiency:** Models based on physical principles often require less data to train, as they rely on prior knowledge of the system being modeled. This can be particularly advantageous in situations where data is scarce or expensive to collect, such as during vehicle operation where conditions are rarely ideal.

- **Robustness:** Models based on physical principles are often more robust to changes in the input data or the environment, as they are based on fundamental laws and principles that do not change over time. This can be particularly important in applications where the

model must operate reliably in a changing or uncertain environment. The automotive application is one of pronounced uncertainty, with highly variable battery conditions and power demands.

Step 2: As part of deciding the model structure, the specific conditions in which the model will operate must be decided. The data a model is designed to work with will fall into one of two categories: small-signal (linear) data restricted to a small region near a steady-state operating point or large-signal (non-linear) data which can encapsulate the entire range of nonlinear lithium-ion battery behavior.

- **Small Signal Data & Models:** In battery modeling, small-signal data are measurements of the battery's terminal voltage in response to small changes in the input variables, such as small perturbations to a constant charge or discharge current. The magnitude of this constant current is large compared to the perturbation magnitude. Small-signal data is typically collected around a certain operating point (fixed state-of-charge, fixed temperature, fixed DC load) and it is used to develop or validate the small-signal model of the battery. A small-signal model of a lithium-ion battery is a linearized approximation of the battery's behavior around a certain operating point. A small-signal model typically consists of a set of linear differential equations that relate the small-signal perturbations in the battery's voltage, current, and other relevant variables. Small-signal models are primarily useful for characterizing a battery's dynamic response about different operating points.

- **Large Signal Data & Models:** In battery modeling, large-signal data are measurements of the battery's terminal voltage in response to significant changes in input variables like charge or discharge current. This data is collected under extreme conditions, such as high-current discharging, very high or low temperatures, and low states-of-charge. One use of this data is developing and validating large-signal battery models that can perform under such conditions, enabling BMSs to simulate and predict the battery's behavior during fast charging or discharging. This information can be used to optimize energy flow in and out of the battery via the BMS's energy management algorithms.

Step 3: Now that the model structure and operating conditions have been decided upon, the data used for estimating the parameters of the model must be chosen. The fundamental choices available to a designer are time domain data and frequency domain data.

- **Time Domain Data:** This data consists of measurements of the battery's behavior over time, commonly recorded as a time series of voltage, current, and temperature measurements. Time domain data illustrates how the battery responds to different

operating conditions and can be used to build models that capture the dynamics of the system.

- **Frequency Domain Data:** This data consists of measurements of the battery's behavior in the frequency domain, which is a mathematical representation of the signal's frequency components. This data is typically obtained by using electrochemical impedance spectroscopy (Appendix B). Frequency domain data can be used to analyze the harmonic components of the battery's impedance, which is a measure of the battery's resistance to the flow of AC current. Measuring the impedance characteristics of the battery using impedance spectroscopy can provide a model designer insights into the battery's state-of-charge, state-of-health, and other hard-to-measure parameters.

Step 4 (not pictured in figure 10)**:** As explored in the *Challenges in Estimating Battery Behavior* section above, the voltage response of lithium-ion batteries is non-linearly dependent on the current applied to the battery. This current dependence also changes with multiple other variables which vary on different time scales, such as temperature, state-of-charge, and state-of-health. Any model attempting to simulate and predict the battery's voltage response must account for this current dependence that varies as the battery operates. To do so, the parameters of the chosen battery model must be updated periodically during operation based on logged (saved to microprocessor memory) and live sensor data. This parameter update process is called 'parameter estimation' and there are many established methods of doing so. These methods are not the focus of this thesis, but for the interested reader, most modern parameter estimation methods are discussed in this comprehensive literature-review [24].

A Minimal Nonlinear Circuit Model of a Lithium-Ion Cell

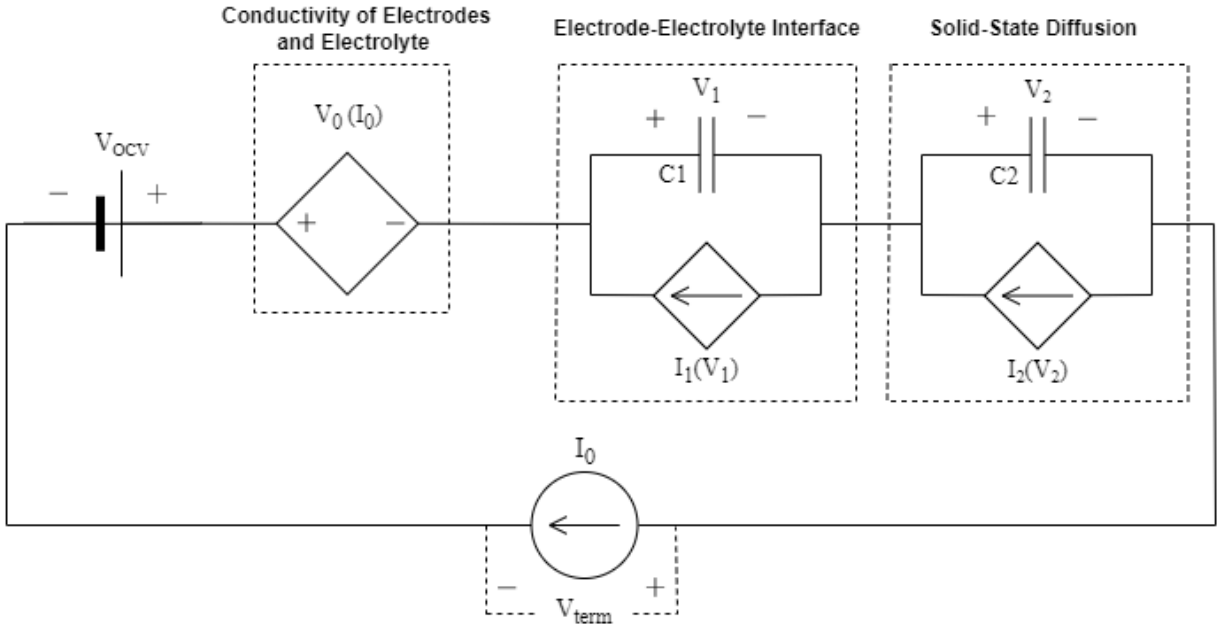

Figure 11: The selected nonlinear circuit for estimating lithium-ion battery behavior.

The model structure shown in figure 11 is a slightly modified version of the reference model developed in [25]. All mentions of the 'nonlinear model' from now on refer to the model in figure 11, and all mentions of the 'reference model' refer to the model from [25]. The researchers who describe the reference model fail to draw a diagram of it and only describe it mathematically, hence why no diagram is shown here for comparison. The primary difference between the reference model and the model in figure 11 is that the dependent sources in figure 11 have taken the place of the variable resistors used in the reference model. This is mostly a matter of semantics and does not significantly change the mathematical structure of the model. The reference model was chosen primarily because it considers the 3 dominant electrochemical processes identified in the *Challenges in Estimating Battery Behavior* section above. Another reason for choosing it was that the researchers in [25] show it performs well when fit to experimental pulse discharge data, with its estimated terminal voltage deviating no more than 50mV from the measured terminal voltage on a series of 60 second discharge pulses of various magnitude.

Representing the Electrode-Electrolyte Interface

At the interface between each electrode and the electrolyte in a lithium-ion cell, charge is transferred according to the Butler-Volmer equation shown below [20]. One electrode usually limits (controls) this reaction, therefore one instance of the Butler-Volmer equation is assumed to be sufficient to represent the charge transfer reaction in the cell.

$$i = FKC^{\alpha_a}\left(C_{s,max} - C_{s,R_p}\right)^{\alpha_a}\left(C_{s,R_p}\right)^{\alpha_c}\left[exp\left(\frac{\alpha_a F\left(\phi_1 - \phi_2 - V_0\right)}{R_G T}\right) - exp\left(-\frac{\left(1-\alpha_c\right)F\left(\phi_1 - \phi_2 - V_0\right)}{R_G T}\right)\right] \quad (1)$$

Where i is the current flowing between the electrode and electrolyte (the charge transfer current), ϕ_1 and ϕ_2 are the solid and liquid phase potentials of the electrode with the overpotential being given by (ϕ_1 - ϕ_2 - V_0), K is the rate constant, $C_{s,Rp}$ and $C_{s,max}$ are the solid lithium concentrations at the surface of an electrode particle and its maximum value respectively, C is the electrolyte concentration, F is Faraday's constant, R_G is the ideal gas constant, T is the temperature in Kelvin, and the transfer coefficients α_a and α_c are typically taken to be 0.5.

If we represent the overpotential as the voltage drop V_1 across capacitor C_1 in the circuit model above, the Butler-Volmer equation can be rewritten as:

$$i = i_0\left[exp\left(\frac{FV_1}{2R_G T}\right) - exp\left(-\frac{FV_1}{2R_G T}\right)\right] \quad (2)$$

where i_0 is the exchange current density, which is the combination of the leading terms in (2), representing the rate of the electron transfer at an electrode surface when the net current is zero. In other words, it is the current density at which the rate of the oxidation reaction (anode) is equal to the rate of the reduction reaction (cathode), so there is no net electron transfer between the electrode and the solution.

Using hyperbolic trigonometric identities, (3) can be simplified as:

$$i = 2i_0 \sinh(\eta); \quad \eta = \frac{FV_1}{2R_G T} \quad (3)$$

To which we add the estimated parameters r_{10} and r_{11} which are identified by fitting the nonlinear model to experimental data using Matlab's nonlinear least squares optimization method in the Parameter Estimator App. Note that the leading constants have been absorbed into r_{10}. This completes the expression for the voltage-dependent current source $I_1(V_1)$:

$$I_1(V_1) = r_{10}\sinh(r_{11}\eta) \quad (4)$$

Representing the Conductivity of the Electrodes and the Electrolyte

Using Raman spectroscopy on $LiMn_2O_4$ spinels, a material used in the cathode of many commercial lithium-ion cells, researchers have found that the level of intercalation in the cathode

of lithium-ion cells can influence the electronic conductivity of the electrode [19]. Furthermore, the concentration of the electrolyte is known to affect the ionic conductivity in the cell [20]. Both the level of intercalation in the electrodes and the concentration of the electrolyte change as a cell charges or discharges. This leads us to the assumption that the electrode electric conductivity and electrolyte ionic conductivity can be represented together by a series voltage-dependent voltage source, $V_0(I_o)$. This source can be described by the following expression:

$$V_0(I_0) = r_0|I_0|^{1-r_1} \quad (5)$$

Where r_0 and r_1 are parameters identified by fitting the model to experimental data with the nonlinear optimization technique of choice. It must be noted that the $(1-r_1)$ term does not need to be in this form for any particular reason. It would simplify the model structure (at least superficially) to write the exponential term as r_1 but this $(1-r_1)$ term was kept anyways to preserve the structure of the reference model, minimizing the chances of the model failing for some unforeseen reason. The reference model uses this form of the exponential term because it comes from the general mathematical form of a variable resistor, the circuit element which the reference model is primarily based around.

Representing Solid-State Diffusion

In the context of lithium-ion batteries, solid-state diffusion refers to the diffusion of lithium ions through a solid-state electrolyte that separates the two electrodes. To indirectly represent this process, we use the fact that solid-state diffusivity varies with ion concentration [4]. We will represent this concentration dependence as a voltage dependence in the circuit model as:

$$I_2(V_2) = r_{20}|V_2|^{1-r_{21}} \quad (6)$$

Circuit Equations

We use Kirchhoff's voltage law to write the conservation of energy for the above circuit:

$$V_{term} = V_{OCV} - V_0(I_0) - V_1 - V_2 \quad (7)$$

And use Kirchhoff's current law to describe the current flowing around the circuit:

$$I_0 = C_1\frac{dV_1}{dt} - I_1(V_1) = C_2\frac{dV_2}{dt} - I_2(V_2) \quad (8)$$

Here it should be mentioned that the V_{OCV} term (open-circuit voltage) is assumed to be known in this model. This poses an issue for working with the model, as open-circuit voltage is not a

directly measurable value when a battery is under load. A simple way to handle this is to measure the cell's terminal voltage at rest and integrate the current flowing into or out of the cell during operation. This integrated current can be used as an input to a lookup table to get OCV. More details on how exactly this can be done are found in the *Nonlinear Model Results* section below.

State Space Equations

We want to represent the behavior of this circuit in state space model form as follows:

$$\frac{\mathrm{d}\vec{x}}{\mathrm{d}t} = f(\vec{x}, u)$$
$$y(t) = g(\vec{x}, u)$$

where x is the state vector, u is the input vector, y is the output vector, and f and g are nonlinear functions. In our case:

$$\vec{x} = \begin{bmatrix} V_1 & V_2 \end{bmatrix}^T; \quad u = I_0; \quad y = V_{term}$$

So the state evolution equations (11) (12) and output equation (13) are written as follows:

$$dV_1/dt = \left(I_1(V_1)/C_1\right) + \left(r_{12} I_0/C_1\right)$$
$$dV_2/dt = \left(I_2(V_2)/C_2\right) + \left(r_{22} I_0/C_2\right) \quad (9)\ (10)$$

$$V_{term} = V_{OCV} - V_0(I_0) - V_1 - V_2 \quad (11)$$

Where r_{12} and r_{22} are additional estimated parameters that were found to help Matlab's nonlinear least squares optimization method achieve more accurate model response. Once expanded is:

$$dV_1/dt = \frac{r_{10}\sinh(r_{11}\eta) + r_{12} I_0}{C_1} \quad (12)$$

$$dV_2/dt = \frac{r_{20}|V_2|^{1-r_{21}} + r_{22} I_0}{C_2} \quad (13)$$

$$V_{term} = V_{OCV} - r_0 |I_0|^{1-r_1} - V_1 - V_2 \qquad (14)$$

Nonlinear Model Results

Nonlinear Model Implementation

See Appendix C for a block diagram of the implemented Simulink model.

The Dataset

The first step towards getting the nonlinear model in figure 11 to emulate the behavior of a real lithium-ion battery was finding an appropriate dataset on which the model could be fit. The 'Randomized Battery Usage 1: Random Walk' dataset from NASA's open data portal [26] was selected because it satisfied the following two requirements.

1. **Contains pulse discharge data with long rest periods:** Pulse discharge data is particularly useful when trying to characterize the voltage response of a lithium-ion cell because the stepped load provokes a pronounced nonlinear voltage response where distinct areas of the response correspond to different physical processes occurring in the cell, as seen previously in figure 4. This helps in achieving a primary goal of this thesis - investigating the interpretability of the model. The pulse discharge experiment data consists of a 1A load applied for 10 minutes followed by 20 minutes of no load. The long rest periods between pulse discharges are also important as these periods allow the battery to reach approximately OCV between pulses, meaning the parameter V_{ocv} is known before and after each pulse discharge. OCV is a continuously varying external parameter in the model that must be known accurately or else the contributions of the other components of the model to V_{term} may be skewed.

2. **Contains low current discharge data for calculating V_{ocv}:** In order to calculate OCV continuously while fitting the nonlinear model to the pulse discharge data, a relationship between the integrated current and the corresponding OCV was required. The dataset contains an experiment called 'low current discharge at 0.04A' where the battery under test was subject to a continuous 0.04A discharge current, taking it from 100% SoC to 0% SoC. This very slow discharging of the battery ensures that the nonlinear dynamics of the battery are not triggered, meaning the measured terminal voltage of the battery is approximately equal to the OCV. This allowed a one-to-one relationship to be found between integrated current and OCV.

3. **Contains variable magnitude pulse discharge data:** To explore the generalizability of the nonlinear model (one of the goals of this thesis), the dataset had to have data from

pulse discharge tests of various magnitudes. The majority of the dataset consists of this, and the experiments of interest are titled ‘discharge (random walk)’. In these random-walk experiments, a charging or discharging current is selected at random from the set {-4.5A, -3.75A, -3A, -2.25A, -1.5A, -0.75A, 0.75A, 1.5A, 2.25A, 3A, 3.75A, 4.5A}, applied for 5 minutes or until the measured terminal voltage goes outside the range (3.2V - 4.2V), then a new current is selected at random and applied to the battery. Negative currents mean charging and positive currents mean discharging. In this thesis, only discharge tests are used in order to limit the scope of the experiments. The nonlinear model was fitted to pulse discharges of 1A, 1.5A, 2.25A, and 3.75A to determine how well it performs at each of these discharge magnitudes.

Every experiment in the dataset contains a time-series of terminal voltage, current, and temperature measurements. This data is sampled every second for the pulse discharge experiments and every 10 seconds for the low current discharge experiment. Multiple lithium-ion cells were tested in this dataset, but the cell named ‘RW9’ is the cell from which all the experimental data used in the following experiments came.

Continuous Determination of Open Circuit Voltage

The nonlinear model shown in figure 11 takes the OCV as one of its parameters to estimate the terminal voltage response. Therefore, the OCV had to be known continuously throughout the fitting procedure. The first step in achieving this was integrating the current at each time step in the ‘low current discharge at 0.04A' to create a table correlating cumulative current to OCV. This by itself was not enough to calculate OCV during the pulse discharge tests though because higher discharge rates inherently cause a significant portion of the current to be dissipated through the internal resistances of the battery caused by the combined resistances of the charge transfer reaction, solid-state diffusion, and electrode and electrolyte resistances among other transient dynamics. In order to account for this, the integrated current was multiplied by a constant (V_ocv_tuner) that was tuned such that the final OCV in the simulation matched the final real OCV, as measured after the 20 minute rest period. This tuning constant increases in size as the magnitude of the discharge current increases, which makes sense as more energy is lost through the internal cell resistances at higher discharge rates. This relationship over 3 discharge current levels is shown in figure 12b below. The piece of the Matlab model which calculates OCV is shown in figure 13.

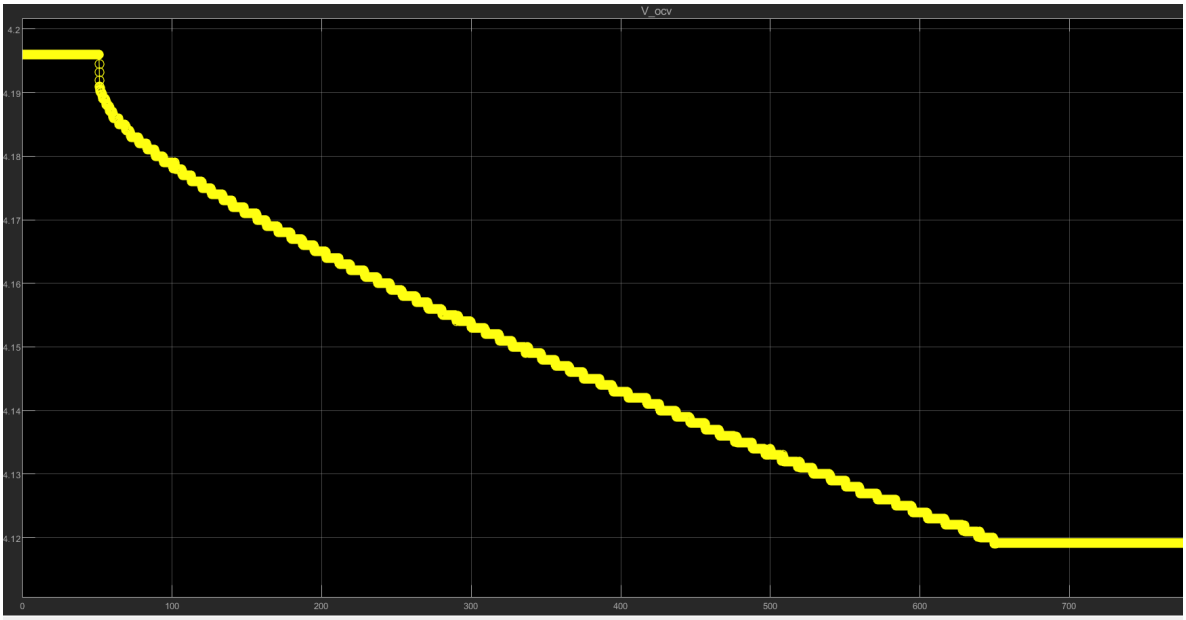

Figure 12a: Calculated open-circuit voltage over the 1A pulse discharge on which the nonlinear model was fit. This was fed into calculation for V_{term} during the model fitting process. The actual final OCV as found in the NASA dataset is 4.119V.

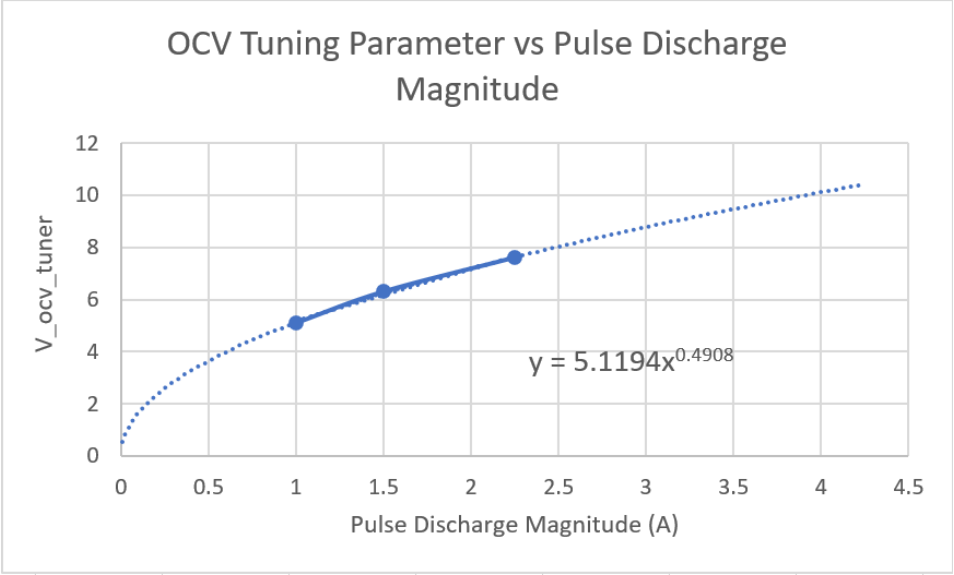

Figure 12b: V_ocv_tuner parameter value trendline after fitting the nonlinear model to pulse discharge data of 1A, 1.5A, and 2.25A. The equation for the best-fit trendline is shown in the middle of the plot. The y-intercept of this trendline is reasonable considering the tuning parameter should be equal to 1 at very low current discharges, as losses through the internal cell resistances are negligible at very low current.

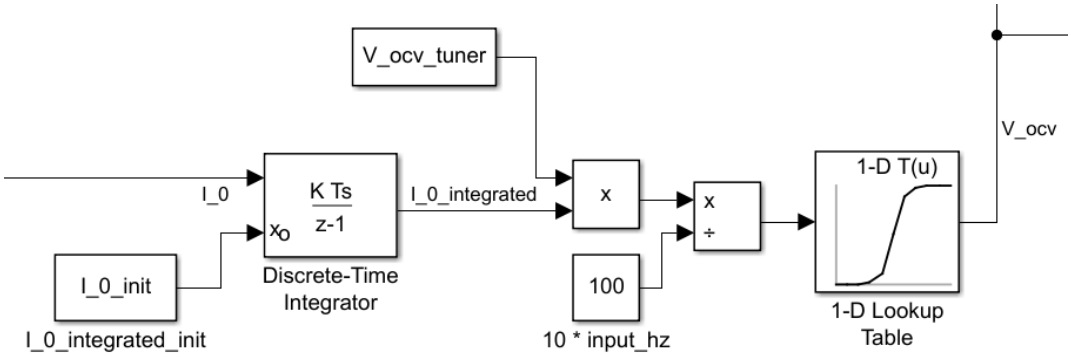

Figure 13: Simulink implementation of the open-circuit voltage calculation for use in the nonlinear model. The division by 100 comes from the fact that the discrete-time integrator is run with a sample rate of 10 Hz but the data in the 'low current discharge at 0.04A', from which the lookup table was generated, is sampled at a rate of 0.1 Hz.

Nonlinear Model Fitting Procedure Using 1A Pulse Discharge Data

All optimization of the nonlinear model was done using Simulink's Parameter Estimator App with the nonlinear least squares routine. The solver used was 'ode15-stiff'. The key setting used while fitting was the 'variable step size' option which automatically shortens the step size of the solver and samples the data at a higher rate when values are changing quickly in order to give those areas sufficient weight during optimization as compared to the 'stiff' regions of the data where things are changing slowly for long periods.

Initial parameter values for the nonlinear model were taken from the best parameter set tested by the researchers who developed the reference model [25]. These initial values produced poor results, as shown in the figures below. Figure 14 shows the voltage response generated by the nonlinear model ('simulated' in the legend) compared to the measured voltage response from the first 'pulsed load' test in the RW9 data, which consists of a 10-minute 1A discharge pulse followed by a 20-minute rest period. Figure 15 shows the 'residuals' generated by this simulation run. The residuals are the differences between each simulated terminal voltage point and the corresponding measured terminal voltage point. The initial parameters were not close to anything resembling a global minimum as further attempts at optimization using the nonlinear least squares routine resulted in negligible improvement. This illustrates the non-negligible differences between the reference nonlinear model and the nonlinear model developed in this thesis.

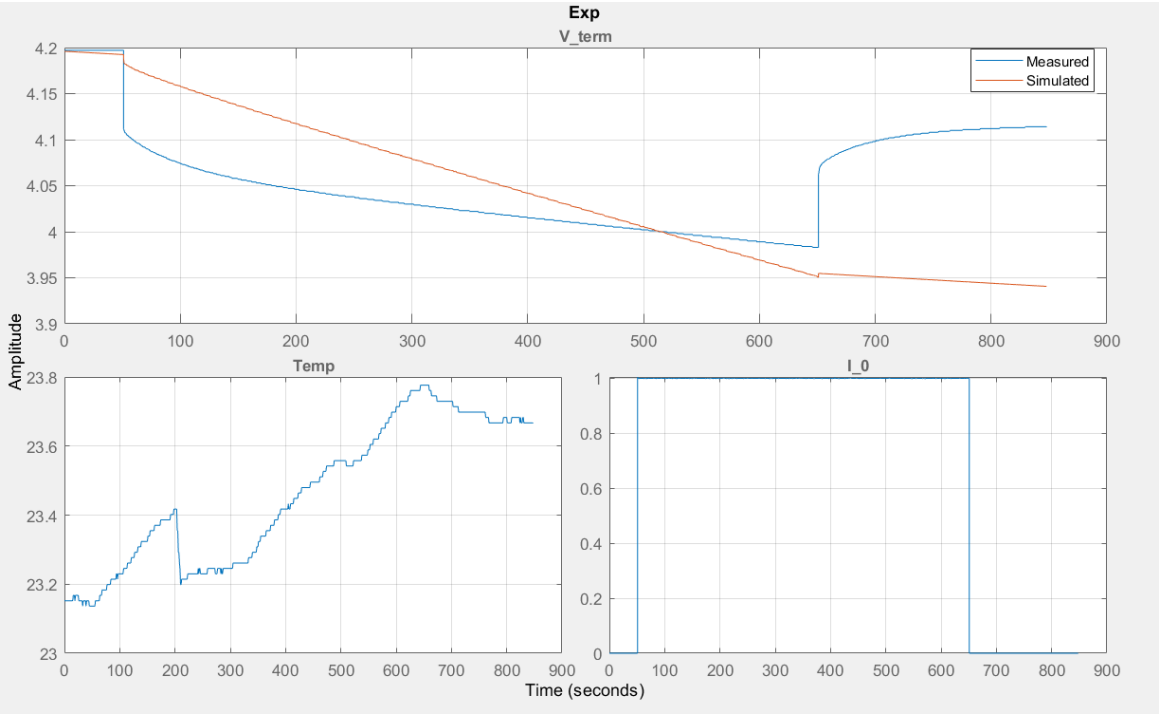

Figure 14: Nonlinear model response using initial parameters from the reference model [25].

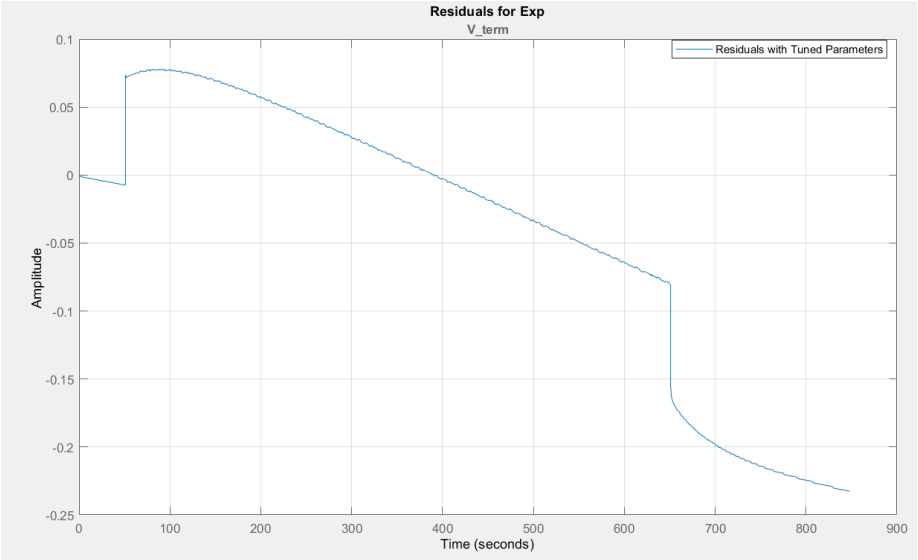

Figure 15: Residuals of the nonlinear model response shown in figure 14.

In an attempt to get the initial values of the model closer to a global minimum such that the nonlinear least squares optimizer could work properly, the responses of each equation representing an electrochemical process were inspected and tuned iteratively by hand. First, noticing that the initial voltage drop due to the resistances of the electrodes and the electrolyte was too small, this was increased until it fell just above the start of the characteristic exponential

curve of the charge transfer reaction. Next, noticing that the contribution of solid-state diffusion was too large (slope of the middle linear region too steep), this was reduced to level off the 'trough' of the curve, if you will. From here, Simulink's nonlinear least squares routine was more successful in fitting the model to the measured voltage response. The result of this fitting attempt is shown in figure 16, with the corresponding residuals shown in figure 17. Despite this small success, the contribution of the charge transfer reaction was still poor and the simulated voltage response still lacked the characteristic exponential curve on both application and removal of the pulse discharge current. This deviation can be seen clearly by inspecting the residuals plot in figure 17, specifically between 50 seconds and 300 seconds, and again between 650 seconds and the end of the test.

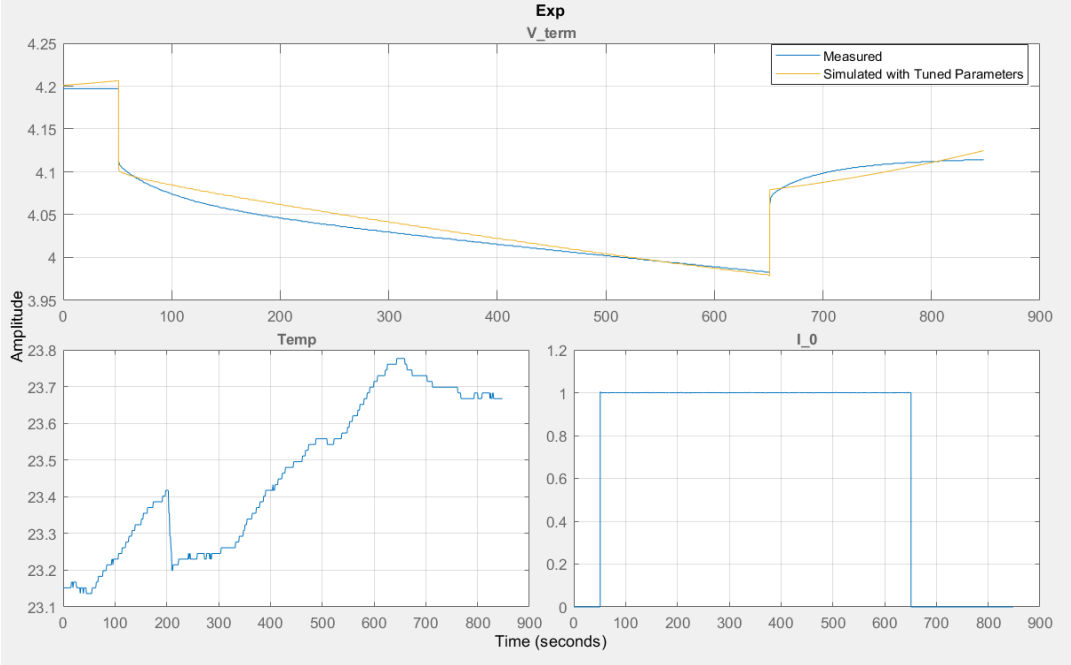

Figure 16: Nonlinear model response after first round of manual tuning and fitting using Matlab's nonlinear least squares routine.

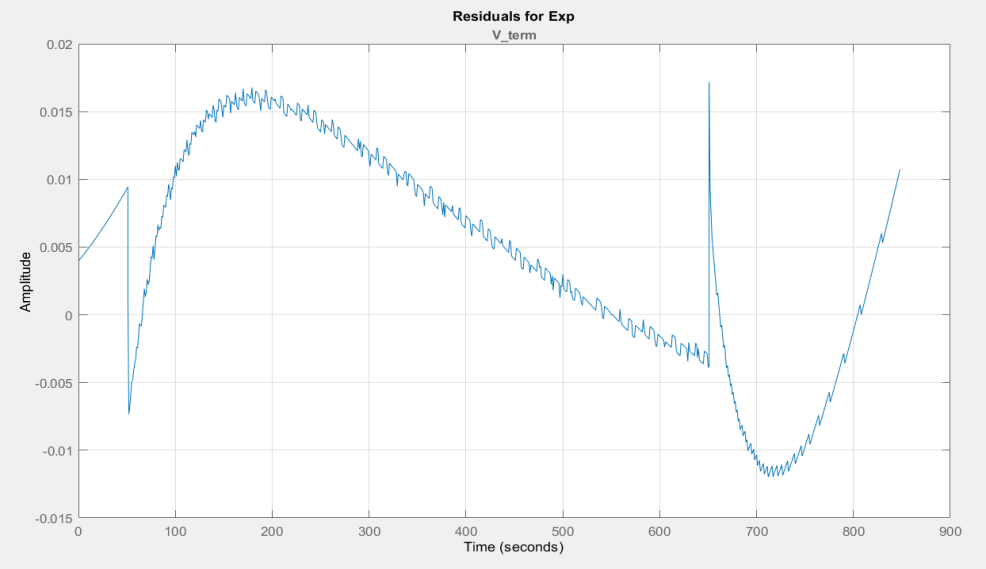

Figure 17: Residuals of nonlinear model response after first round of manual tuning and fitting using Matlab's nonlinear least squares routine.

After comparing the output of the charge transfer reaction equation (4) to the output of dV_1/dt, it became clear that the influence of I_0 in the equation for dV_1/dt (12) was dominating the output. It was here that parameters r_{11} and r_{12} were added to the model in an effort to give Matlab's optimizer more values to play with to maximize the effect of the charge transfer reaction. After estimating the parameters once more, the influence of the Butler-Volmer equation became more pronounced, as seen especially clearly between 0 and 100 seconds in figure 18.

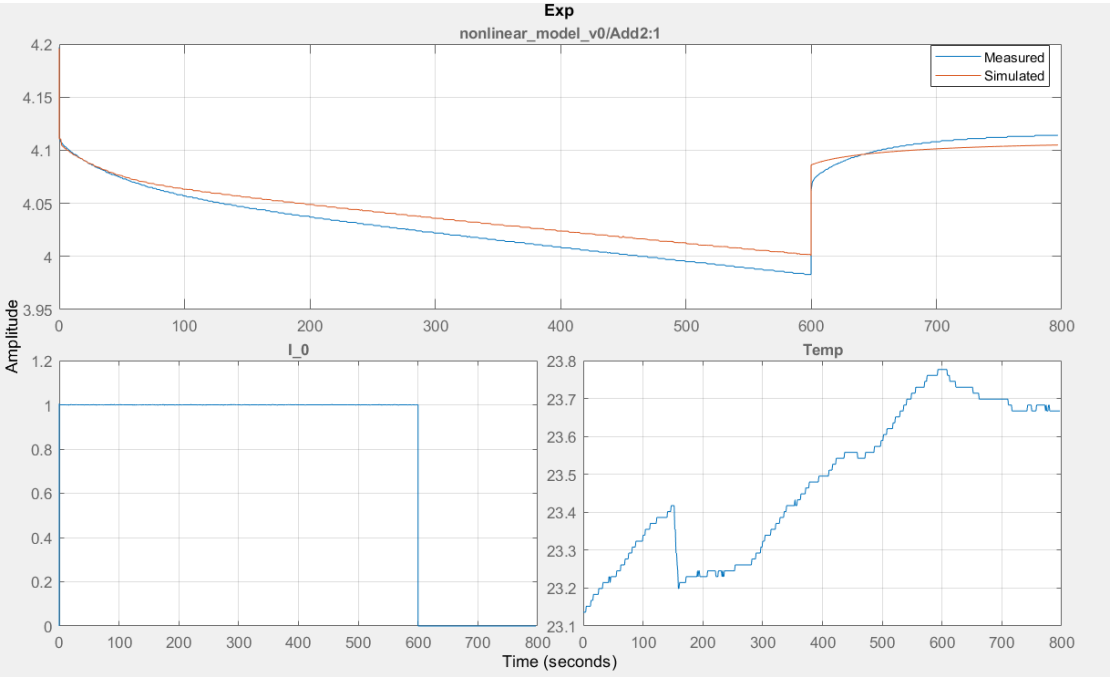

Figure 18: Nonlinear model optimization results after additional parameters were added to equation 12.

To try and optimize further, a closer inspection of outputs of each part of the system was needed.

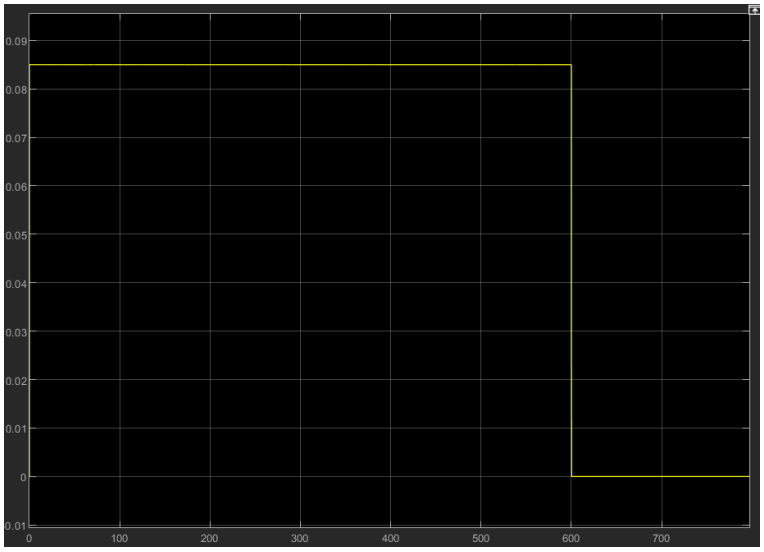

Figure 19: Contribution of electrode and electrolyte resistances to the nonlinear model response shown in figure 18.

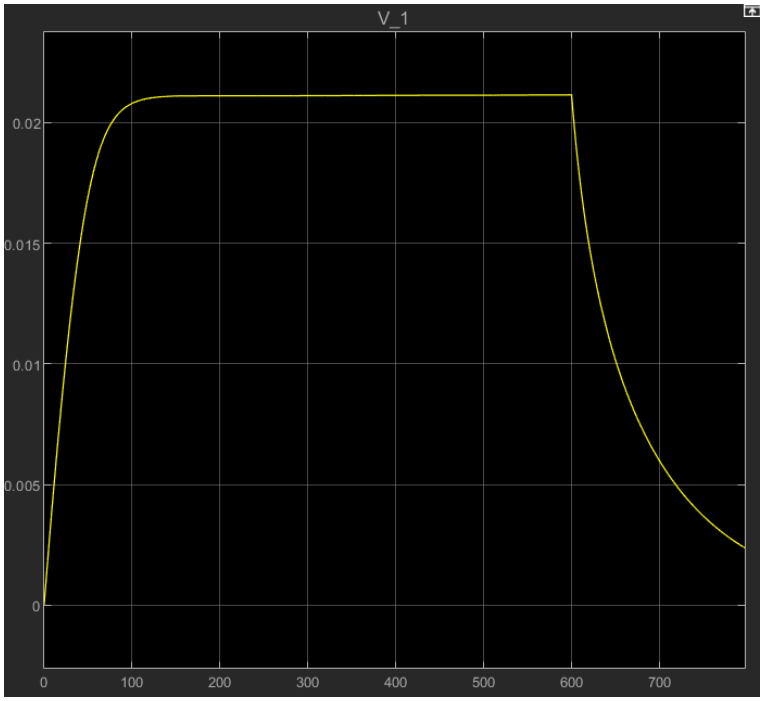

Figure 20: Contribution of the charge transfer reaction (V_1) to the nonlinear model response shown in figure 18.

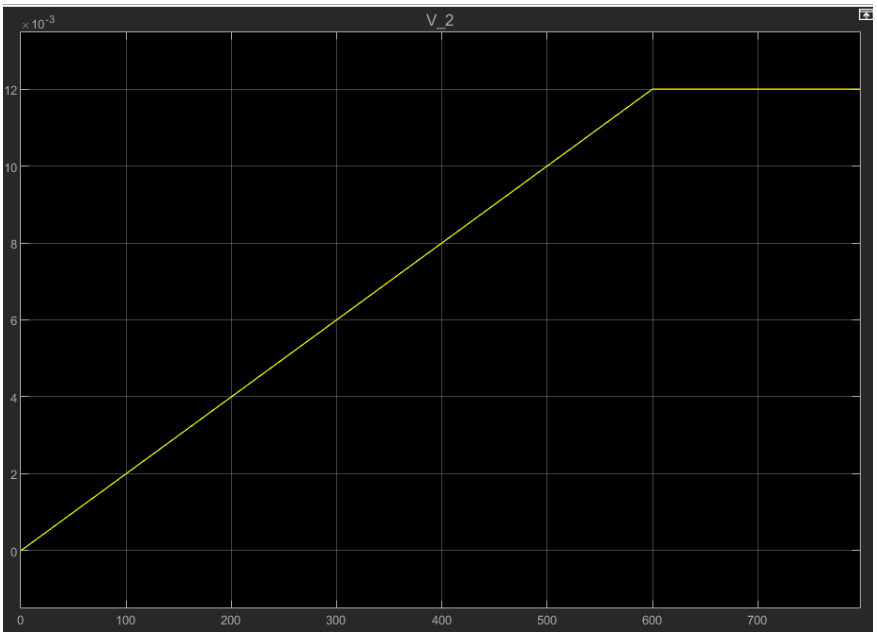

Figure 21: Contribution of solid-state diffusion (V_2) to the nonlinear model response shown in figure 18.

The output of the voltage source V_2, corresponding to solid-state diffusion (figure 21), was being completely dominated by the I_0 term in the numerator of eq. 13. To combat this, another variable, r22, was added to allow the nonlinear least squares optimizer to directly minimize the effect of the I_0 term. The resulting optimization was the best simulated voltage response achieved on the 1A pulse discharge data, as seen in figures 22 and 23.

Final Nonlinear Model Performance on 1A Pulse Discharge Data

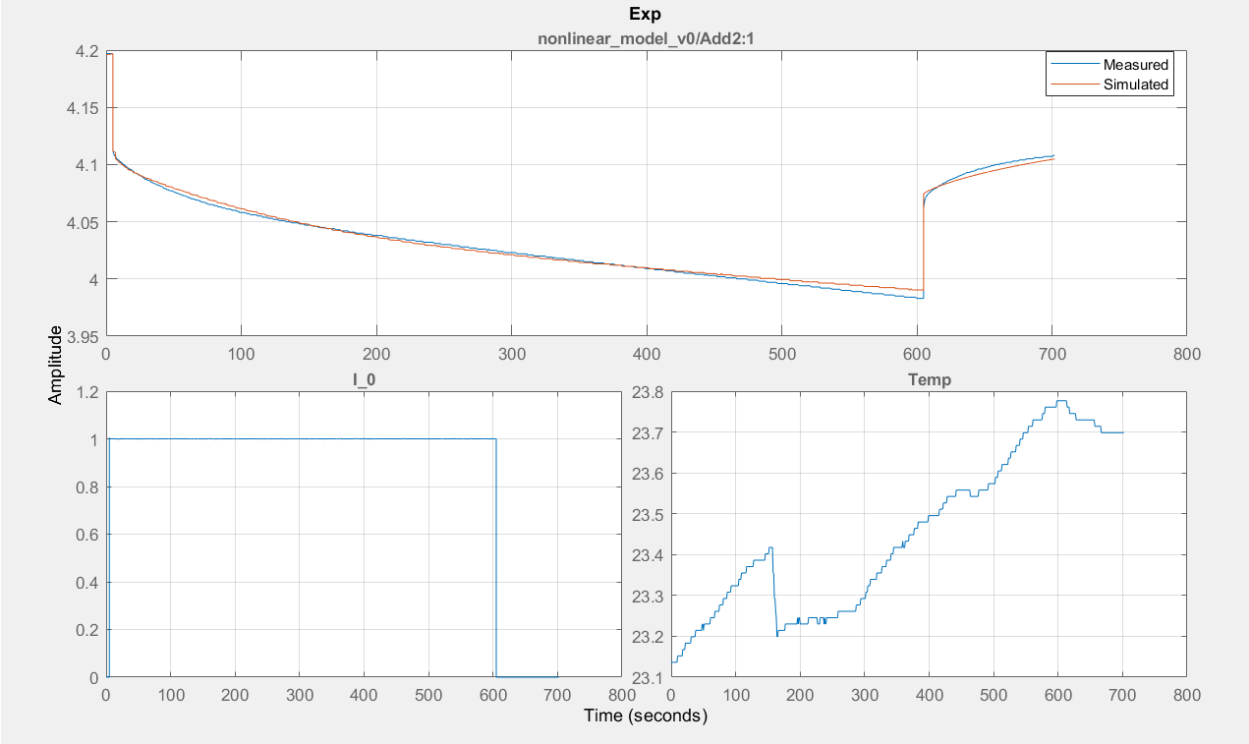

Figure 22: Best simulated voltage response achieved with the nonlinear model on the 1A pulse discharge data.

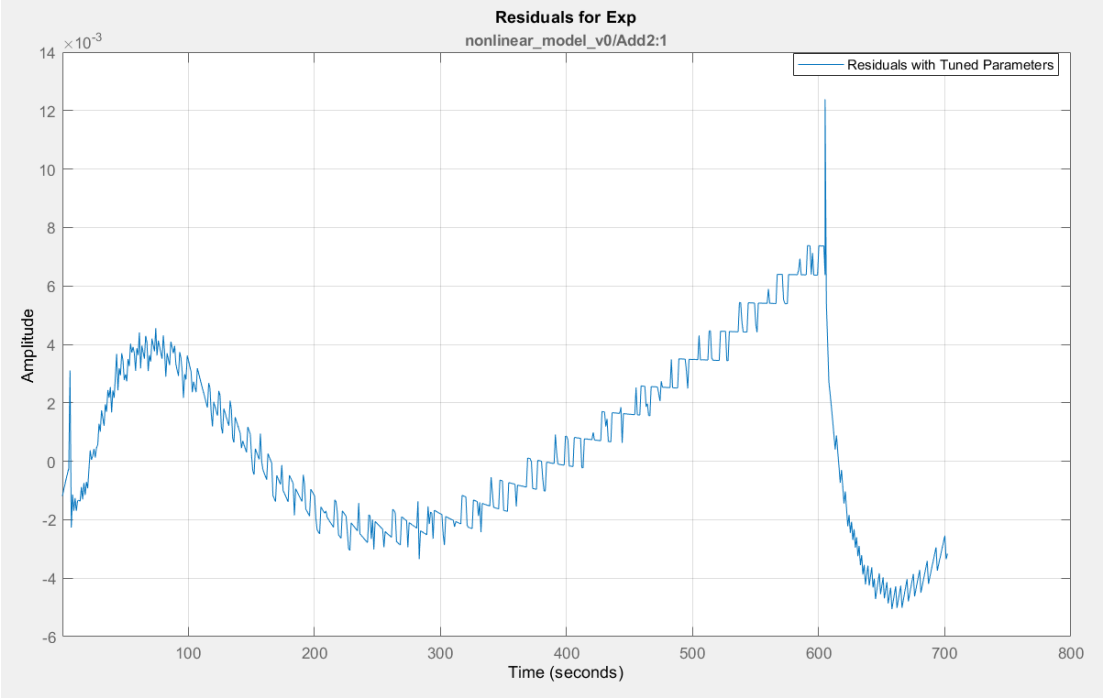

Figure 23: Residuals from the simulation run shown in figure 22.

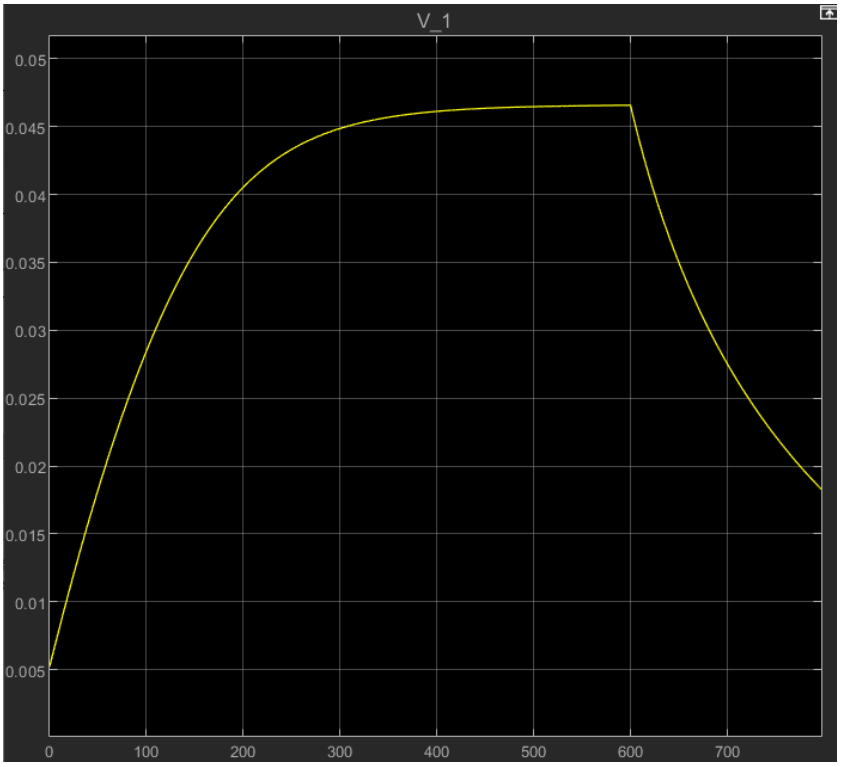

Figure 24: Contribution of the charge transfer reaction (V_1) to the simulated voltage response shown in figure 22.

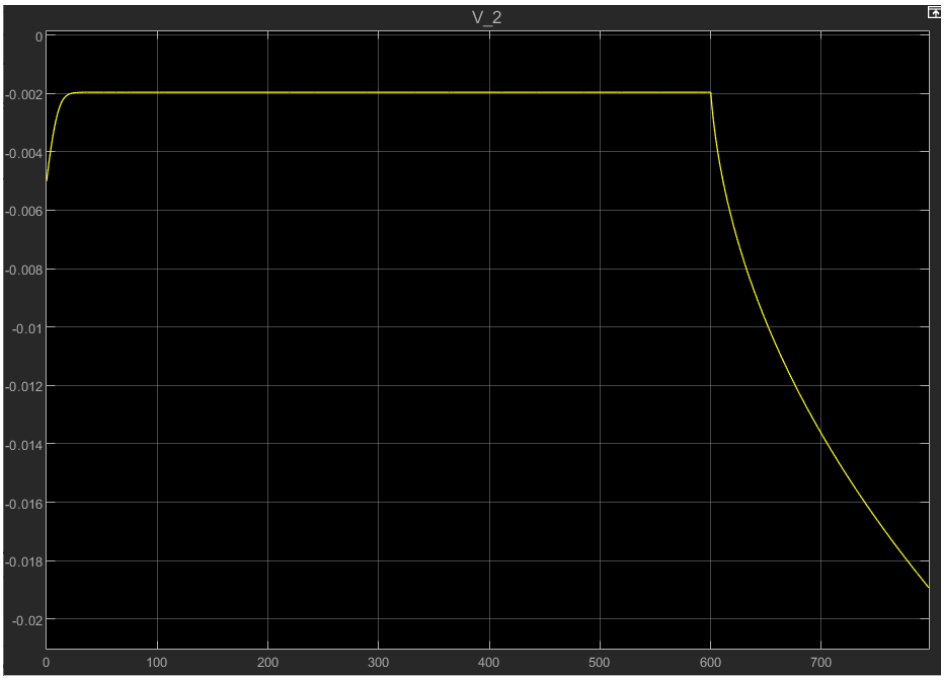

Figure 25: Contribution of solid-state diffusion (V_2) to the simulated voltage response shown in figure 22.

```
C_1_nlin = 30000;
C_2_nlin = 50000;
r_0_nlin = 0.08501145744702633;
r_1_nlin = 0.9526657525808544;
r_10_nlin = 2.516018057644571;
r_11_nlin = -2.201761994124434;
r_12_nlin = 9.186283856823833;
r_20_nlin = -0.03630507227176677;
r_21_nlin = 2.048302576475839;
r_22_nlin = 25;

V_ocv_tuner = 5.1;
```

Figure 26: Parameters used in the nonlinear model to simulate the voltage response seen in figure 22.

Analysis of Nonlinear Model Performance on 1A Pulse Discharge Data

Overall, the fit is quite good, with a peak residual of around 12 millivolts at the point when the load is removed. During the discharge pulse itself, the model's estimated voltage response only deviates from the measured response by a maximum of 4 millivolts at around 80 seconds. In the timescale of interest for power calculations that are informed by the DCR (1-20 seconds [7][8][9]), the maximum deviation is only 2.1 millivolts. This result shows that at least for the 1A pulse discharge data on which the model was fit, the simulated voltage response can be used to accurately determine the DCR.

The contribution of the charge transfer reaction is one aspect of this model that can be confidently classified as interpretable. It is based directly on the Butler-Volmer equation and it behaves as one expects it would - rising in a decaying exponential fashion when the load is applied, leveling off as the reaction reaches equilibrium, and sharply diving into another decaying exponential as the load is removed.

The contributions of solid state diffusion and of the electrode and electrolyte resistances to the simulated voltage response are less confidence inspiring. They are structured as general exponential forms that have no basis in the processes they are attempting to model. The combined electrical resistances of the electrodes and the ionic resistance of the electrolyte is essentially a constant that depends on the magnitude of the input voltage, which seems to be sufficient in this specific case. It should change as the battery discharges but it must be tested on a battery with lower SoC to prove that it actually would. It should also increase as the battery ages, but only an investigation into the model's performance on aged cells could determine if that would happen either. Finally, the contribution of the solid-state diffusion reaction makes no

sense. It should always be greater than zero, yet it seems to always be below zero at this local minimum of the optimization.

To investigate the behavior of the nonlinear model further, we will now test it on experimental data from larger pulse discharges.

Exploring Generalizability of the Nonlinear Model

To verify that the nonlinear model could perform on data other than the 1A pulse discharge test, data from the 'discharge (random walk)' sections of the NASA dataset were used. First, the parameters which resulted in the best simulated voltage response on the 1A pulse discharge test were used in the nonlinear model to simulate the voltage responses corresponding to pulse discharges of 1.5A, 2.25A, and 3.75A. After testing the nonlinear model response at each pulse magnitude with parameters optimized for the 1A pulse discharge, the parameters were re-estimated for each different pulse discharge magnitude individually to see what performance the model can achieve when overfit to the specific data.

Here, the nonlinear model, with parameters optimized for the 1A pulse discharge data, was tested on a 5 minute long, 1.5A pulse discharge from the NASA dataset. The resulting simulated voltage response is shown below in figure 27.

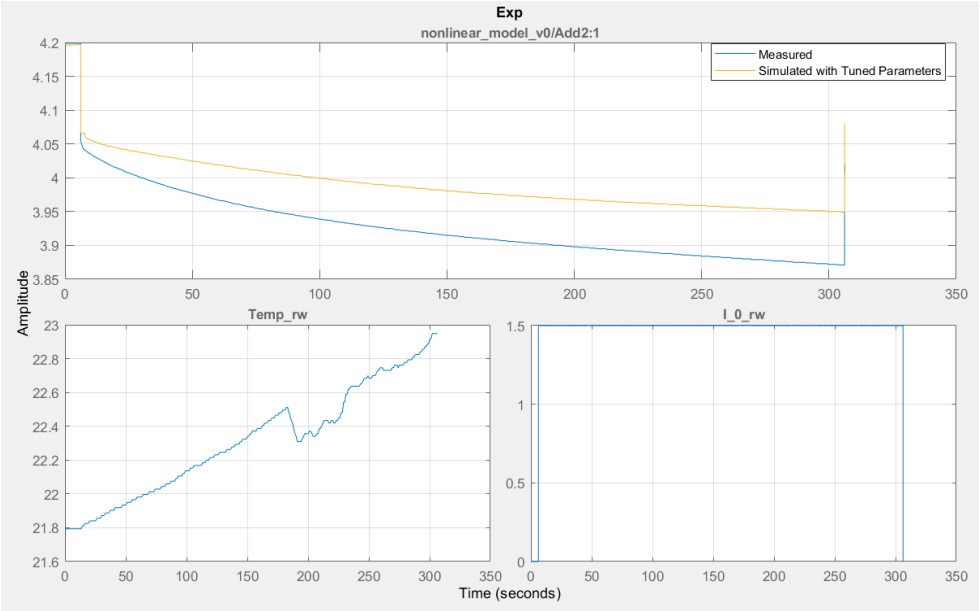

Figure 27: Simulated voltage response to 1.5A pulse discharge from nonlinear model with parameters optimized for a 1A pulse discharge.

This result shows that the parameters found for the 1A pulse discharge do not generalize well to different discharge rates. After using Simulink's nonlinear least squares optimizer on the 1.5A pulse discharge data, the simulated voltage response of the overfit model was much more accurate, as shown in figure 28. The corresponding residuals for this simulated voltage response are shown in figure 29. By examining these residuals, specifically between ~10 seconds and ~100 seconds, we notice that the characteristic exponential shape of the charge transfer reaction is no longer being simulated as accurately.

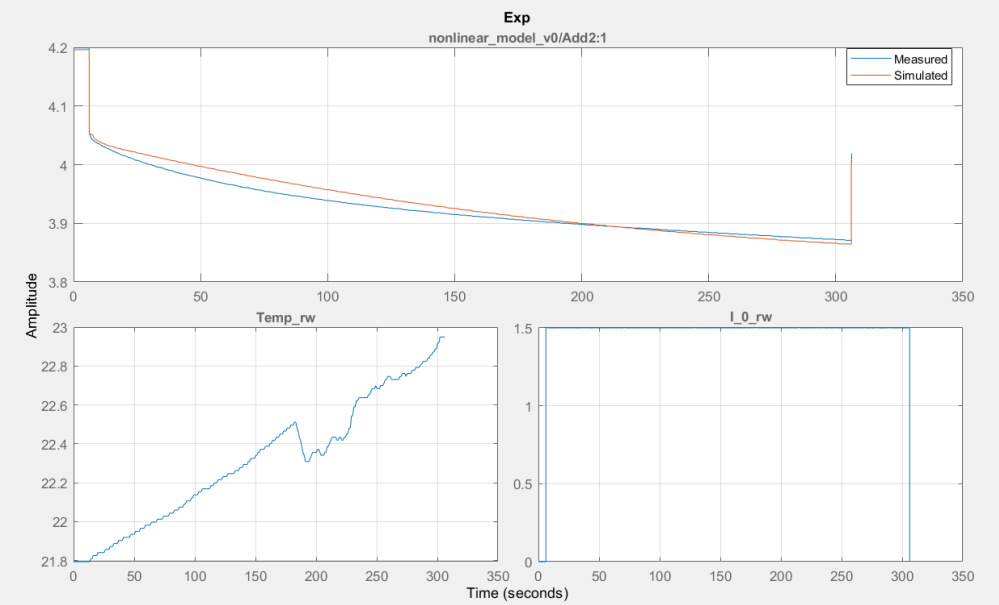

Figure 28: Simulated voltage response to 1.5A pulse discharge using the nonlinear model with parameters optimized for the 1.5A pulse discharge data.

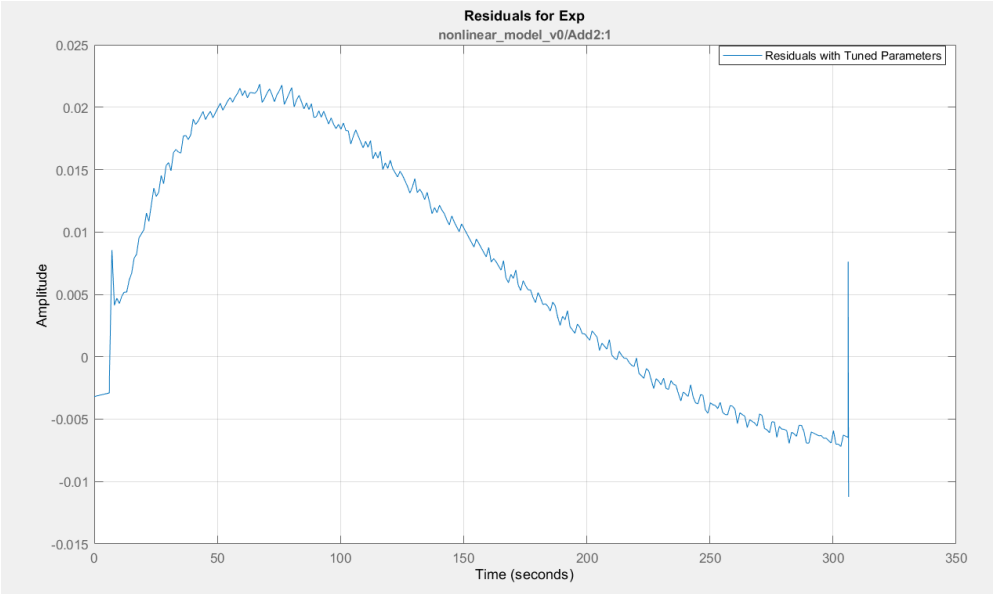

Figure 29: Residuals corresponding to the simulated voltage response in figure 28.

```
C_1_nlin = 30000;
C_2_nlin = 50000;
r_0_nlin = 0.0923002496410146;
r_1_nlin = 0.9526657525808544;
r_10_nlin = 4.93766814739926;
r_11_nlin = -0.89825820723166;
r_12_nlin = 14.3229835374507;
r_20_nlin = -0.185273691167141;
r_21_nlin = 1.41016489190863;
r_22_nlin = 25.7506726263405;

V_ocv_tuner = 6.29451045143225;
```

Figure 30: Nonlinear model parameters used to the simulated voltage response in figure 28.

Next, returning to parameters optimized for the 1A pulse discharge data, the nonlinear model was tested on a 5 minute long, 2.25A pulse discharge from the NASA dataset. The resulting simulated voltage response is shown below in figure 31.

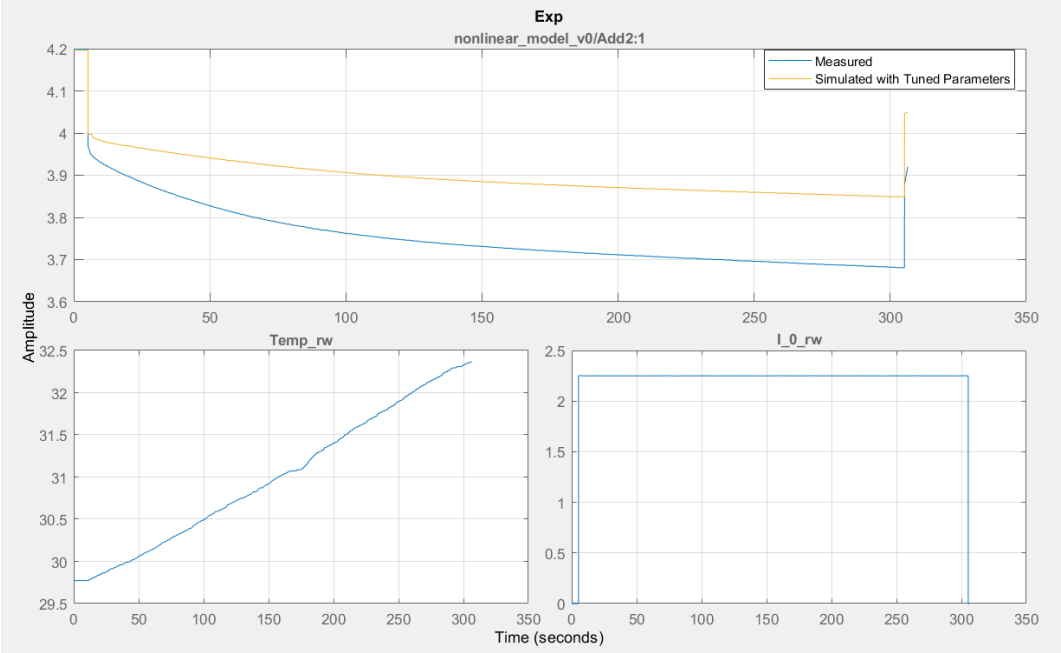

Figure 31: Simulated voltage response to 2.25A pulse discharge using the nonlinear model with parameters optimized for a 1A pulse discharge.

Clearly, the simulated voltage response using these parameters is far off of the measured voltage response. The generalizability of the nonlinear model using the 1A pulse discharge parameters is evidently quite poor. One potential factor in this may be that the OCV tuning parameter (*V_ocv_tuner*) is staying fixed despite the discharge current changing. Simulink's parameter estimator was used to fit the nonlinear model to this 2.25A pulse discharge and the results of this process are shown in figures 32 and 33.

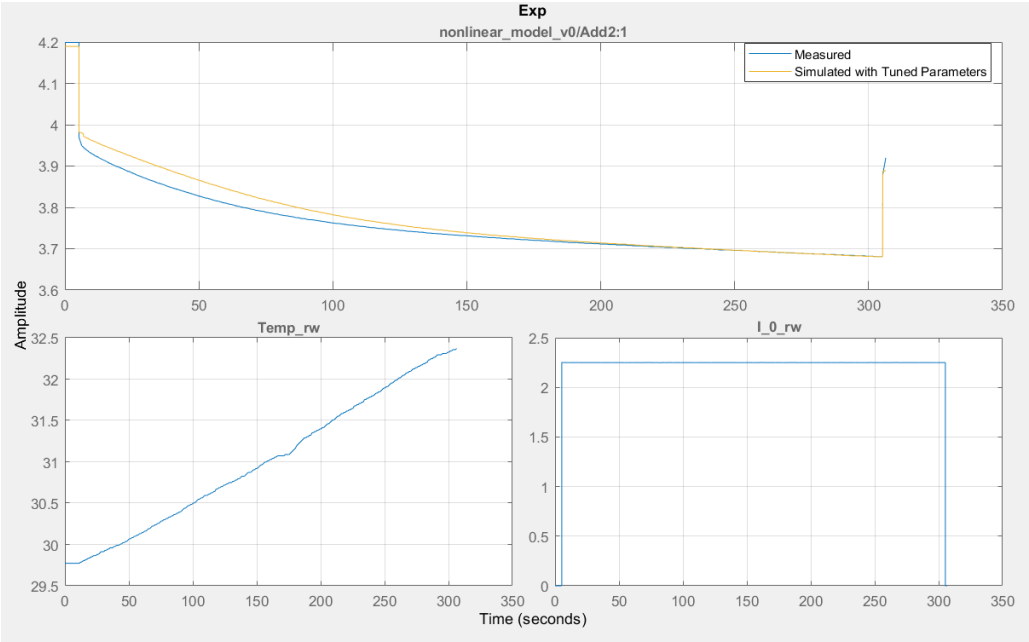

Figure 32: Simulated voltage response to 2.25A pulse discharge using the nonlinear model with parameters optimized for the 2.25A pulse discharge data.

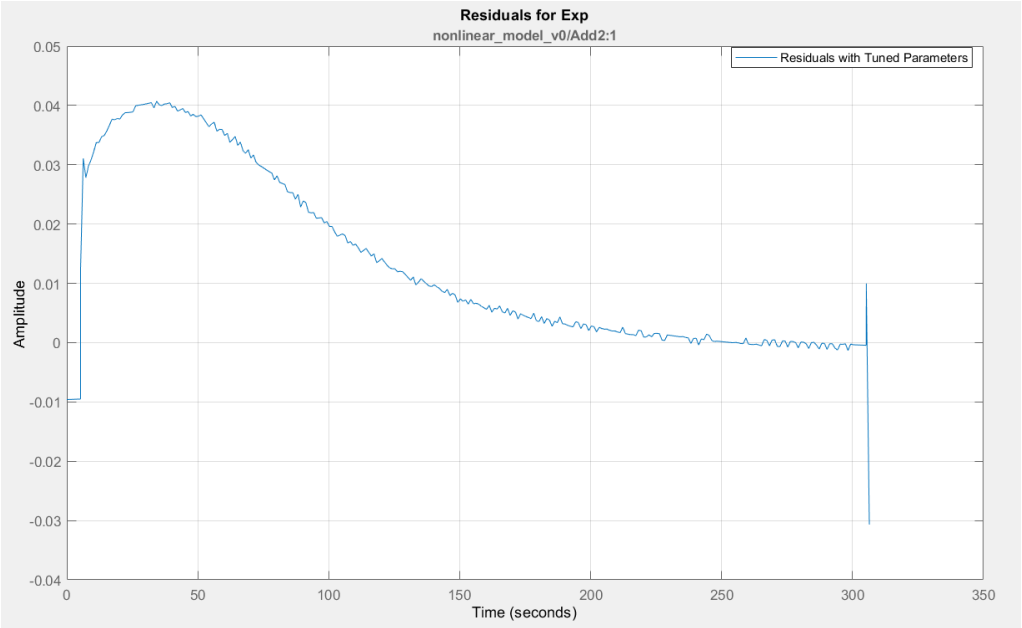

Figure 33: Residuals corresponding to the simulated voltage response in figure 32.

```
C_1_nlin = 30000;
C_2_nlin = 50000;
r_0_nlin = 0.0887088445331997;
r_1_nlin = 0.9526657525808544;
r_10_nlin = 3.53391;
r_11_nlin = -1.46459029718638;
r_12_nlin = 18.3741773137246;
r_20_nlin = -10039.4;
r_21_nlin = -1.3134;
r_22_nlin = 15.5037;

V_ocv_tuner = 7.59341435580328;
```

Figure 34: Nonlinear model parameters used to the simulated voltage response in figure 32.

The maximum residual seen (~40mV) is caused by the charge transfer reaction contribution being too small. This is still a good fit, comparable to the accuracy seen in the reference model (<50mV residuals). Upon inspecting the contribution of the solid-state diffusion in the nonlinear model, an interesting finding arises, as seen in figure 35. The solid-state diffusion now behaves in a sensical manner, always with a positive voltage drop across C_2, which exponentially decreases until it stabilizes to a fixed, positive value. The primary causes for this were parameter r_{20} going from a small negative number to a large negative number (~100 000x bigger), and r_{21} going from a positive number to a negative number. Both of these parameter changes were driven by Simulink's nonlinear least squares optimization routine.

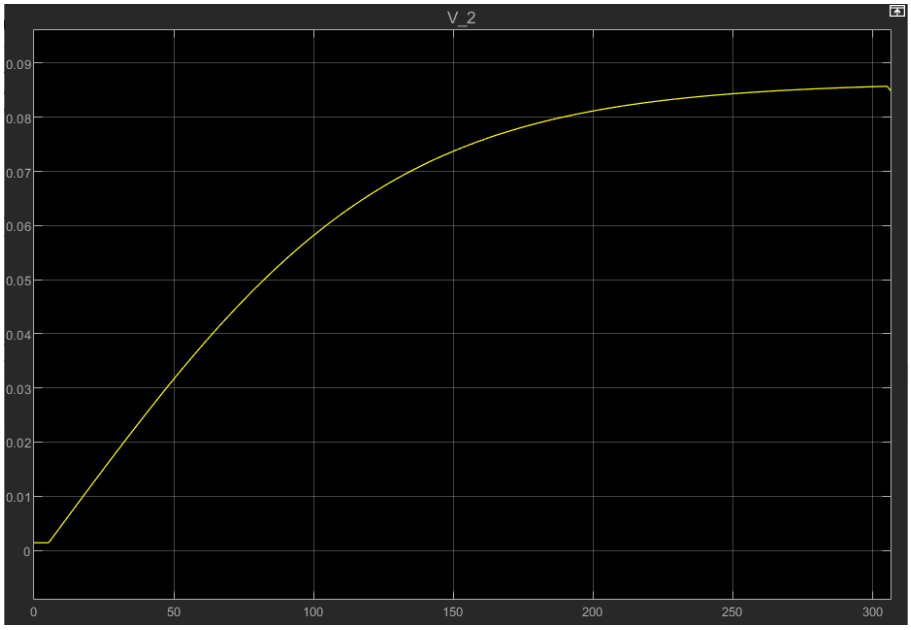

Figure 35: Contribution of solid-state diffusion (V_2) to the simulated voltage response in figure 32.

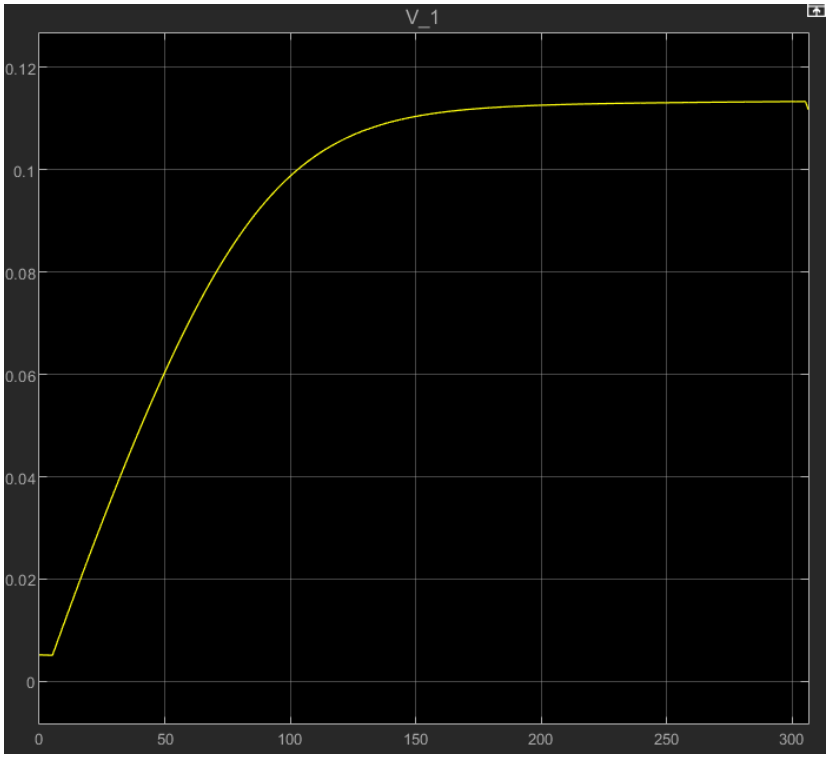

Figure 36: Contribution of the charge transfer reaction (V_1) to the simulated voltage response in figure 32.

Finally, figure 37 shows the model failing to simulate the voltage response to a 3.75A pulse discharge, despite being fit to this 3.75A pulse. This failure may indicate that the nonlinear model has an absolute limit for the magnitude of response it can replicate. Though, this failure could simply be a sign that the parameters were initialized too far from a global minimum for the nonlinear least squares optimizer to optimize effectively.

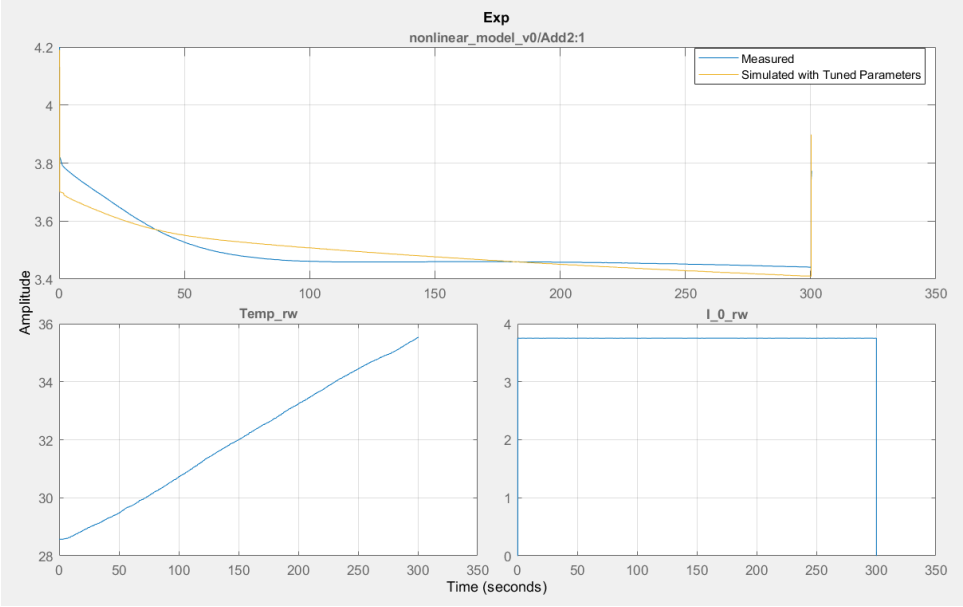

Figure 37: Failure of the nonlinear model to simulate the voltage response to a 3.75A pulse discharge, despite the parameters being optimized for this specific data.

Discussion of Generalization Tests

The results in the above section demonstrate the limitations of the nonlinear model's performance in conditions outside of those in which it was fit. One of the more interesting results is the sudden shift in the contribution of solid-state diffusion (V_2) when the nonlinear model was fit to the 2.25A pulse discharge. The model parameters r_{20} and r_{21} had to change massively in order to trigger this change, and luckily Simulink's nonlinear least squares optimizer was able to do so. Despite the drastic parameter change, the overall behavior of the model did not change drastically. This result illustrates the difficulty in finding a true global optimum for a complex model with many parameters. One set of parameters may be completely different to another, yet the final output of the model using either set may be quite similar! In order to address this in the future, a robust method of initializing the model parameters such that they start as close to the global minimum as possible would be useful. Additionally, an optimization technique which can effectively avoid small local minima as it optimizes would be beneficial.

Linearizing the Minimal Nonlinear Circuit Model

Comparing Nonlinear and Linear Models

Working with nonlinear systems is generally much more difficult than working with linear systems. The following points support this claim and provide motivation for investigating the performance of a linearized version of the above nonlinear circuit model:

- **Superposition:** In a linear system, superposition holds true, meaning the output of the system is proportional to the input. This property allows for straightforward insight into the system as input signal perturbations create predictable output signal responses. Comparatively, small changes to the input signal of a nonlinear system can result in large, unpredictable changes to the output signal.
- **Analytical Solutions:** Linear dynamic systems can often be solved analytically, which means that there are closed-form mathematical solutions that describe the behavior of the system. In contrast, nonlinear systems typically do not have analytical solutions, and numerical techniques must be used to approximate their behavior. Numerical techniques result in approximations of analytical solutions and are typically harder to compute.
- **Computational Complexity:** Nonlinear dynamic systems can be computationally expensive to solve, especially when they involve many variables or complex nonlinearities. This can make it difficult to analyze and simulate the behavior of nonlinear systems, and can require specialized computational techniques and hardware. Linear systems, on the other hand, are easier to solve, largely because they often have an analytical solution as mentioned above.

Linearizing the Nonlinear Model About an Operating Point

The nonlinear model presented above in figure 11 is able to simulate lithium-ion battery behavior under large-signal conditions, meaning it can maintain accurate voltage response estimations through highly dynamic loads and changing SoC. If we wish to gain the benefits of superposition and of the lower computational complexity offered by linear models, we have the option of linearizing the nonlinear model. In doing so, we must consider that the new linearized model will likely not provide accurate behavioral estimates under large-signal conditions, when the load on the battery is high and SoC does not remain constant. By definition, the linearization of a nonlinear model is done about an equilibrium point, therefore the resulting model can only be relied upon within a certain ‘operating range’ of the equilibrium point. The linearized model is known as a small-signal model because it is only accurate for ‘small signals’ within an operating range.

Recall that currently, our nonlinear system is of the form:

$$\frac{\mathrm{d}\vec{x}}{\mathrm{d}t} = f(\vec{x}, u)$$
$$y(t) = g(\vec{x}, u)$$

where x is the state vector, u is the input vector, y is the output vector, and f and g are nonlinear functions. In our case:

$$\vec{x} = \begin{bmatrix} V_1 & V_2 \end{bmatrix}^T; \quad u = I_0; \quad y = V_{term}$$

We want to convert the system equations to the linear form:

$$\frac{\mathrm{d}\vec{x}}{\mathrm{d}t} = \vec{A}\vec{x} + \vec{B}u$$
$$y(t) = \vec{C}\vec{x} + Du$$

Where $\vec{A}$, $\vec{B}$, $\vec{C}$, and D are Jacobians of the respective system equation, evaluated at the equilibrium point around which the linearized model is to be evaluated. The first step in manipulating the nonlinear system equations into the above form is to define a coordinate transformation. Given an equilibrium point:

$$\vec{x}^* = \begin{bmatrix} V_1^* & V_2^* \end{bmatrix}^T \quad (15)$$

Obtained during approximately DC conditions where:

$$u^* = I_0^* \quad (16)$$

We define a coordinate transformation:

$$\Delta\vec{x} = \begin{bmatrix} \Delta V_1 \\ \Delta V_2 \end{bmatrix} = \begin{bmatrix} V_1 - V_1^* \\ V_2 - V_2^* \end{bmatrix} \quad (17)$$

$$\Delta u = \Delta I_0 = I_0 - I_0^* \quad (18)$$

$$\Delta y = \Delta V_{term} = V_{term} - V_{term}^* \quad (19)$$

Substituting our newly parameterized variables into the linear form we're trying to achieve, we get:

$$\frac{\mathrm{d}(\,\Delta\vec{x}\,)}{\mathrm{d}t} = \vec{A}\,\Delta\vec{x} \;+\; \vec{B}\,\Delta u$$

$$\Delta y(\,t) \;= \vec{C}\,\Delta\vec{x} \;+\; D\,\Delta u$$

Where the Jacobian,

$$\vec{A} = \left.\frac{\partial f}{\partial \vec{x}}\right|_{(\,\vec{x}^{\,*},\,u^{*})} = \left.\begin{bmatrix} \dfrac{\partial\left(\dfrac{\mathrm{d}V_1}{\mathrm{d}t}\right)}{\partial V_1} & \dfrac{\partial\left(\dfrac{\mathrm{d}V_1}{\mathrm{d}t}\right)}{\partial V_2} \\ \dfrac{\partial\left(\dfrac{\mathrm{d}V_2}{\mathrm{d}t}\right)}{\partial V_1} & \dfrac{\partial\left(\dfrac{\mathrm{d}V_2}{\mathrm{d}t}\right)}{\partial V_2} \end{bmatrix}\right|_{(\,\vec{x}^{\,*},\,u^{*})}$$

$$\vec{A} = \left.\begin{bmatrix} \dfrac{\partial\left(\dfrac{r_{10}\sinh\left(r_{11}\eta\right) \;+\; r_{12}I_0}{C_1}\right)}{\partial V_1} & \dfrac{\partial\left(\dfrac{r_{10}\sinh\left(r_{11}\eta\right) \;+\; r_{12}I_0}{C_1}\right)}{\partial V_2} \\ \dfrac{\partial\left(\dfrac{r_{20}\left|V_2\right|^{1-r_{21}} + r_{22}I_0}{C_2}\right)}{\partial V_1} & \dfrac{\partial\left(\dfrac{r_{20}\left|V_2\right|^{1-r_{21}} + r_{22}I_0}{C_2}\right)}{\partial V_2} \end{bmatrix}\right|_{(\,\vec{x}^{\,*},\,u^{*})}$$

$$\vec{A} = \left.\begin{bmatrix} \dfrac{\partial\left(\dfrac{r_{10}\sinh\left(\frac{r_{11}FV_1}{2R_GT}\right) \;+\; r_{12}I_0}{C_1}\right)}{\partial V_1} & \dfrac{\partial\left(\dfrac{r_{10}\sinh\left(\frac{r_{11}FV_1}{2R_GT}\right) \;+\; r_{12}I_0}{C_1}\right)}{\partial V_2} \\ \dfrac{\partial\left(\dfrac{r_{20}\left|V_2\right|^{1-r_{21}} \;+\; r_{22}I_0}{C_2}\right)}{\partial V_1} & \dfrac{\partial\left(\dfrac{r_{20}\left|V_2\right|^{1-r_{21}} \;+\; r_{22}I_0}{C_2}\right)}{\partial V_2} \end{bmatrix}\right|_{(\,\vec{x}^{\,*},\,u^{*})}$$

The top-right and bottom-left expressions are canceled out as they don't depend on V_2 and V_1 respectively. The bottom-right expression is evaluated by considering that the sign of V_2 can only change when switching from discharging to charging or vice-versa. Therefore, it can be handled in the model with a simple conditional statement that uses the sign of I_0 as the condition. This gives us:

$$\vec{A} = \left[\begin{array}{cc} \dfrac{r_{10} r_{11} F \cosh\left(\dfrac{r_{11} FV_1}{2R_G T} \right)}{2R_G T C_1} & 0 \\ 0 & \dfrac{(r_{20} - r_{21} r_{20}) |V_2|^{-r_{21}}}{C_2} \end{array} \right] \Bigg|_{(\vec{x}^*, u^*)}$$

Which when evaluated at the equilibrium point, gives us:

$$\vec{A} = \left[\begin{array}{cc} \dfrac{r_{10} r_{11} F \cosh\left(\dfrac{r_{11} FV_1^*}{2R_G T} \right)}{2R_G T C_1} & 0 \\ 0 & \dfrac{(r_{20} - r_{21} r_{20}) |V_2^*|^{-r_{21}}}{C_2} \end{array} \right] \tag{20}$$

The next Jacobian,

$$\begin{aligned} \vec{B} = \left. \frac{\partial f}{\partial u} \right|_{(\vec{x}^*, u^*)} &= \left[\begin{array}{cc} \dfrac{\partial \left(\dfrac{\mathrm{d}V_1}{\mathrm{d}t} \right)}{\partial I_0} & \dfrac{\partial \left(\dfrac{\mathrm{d}V_2}{\mathrm{d}t} \right)}{\partial I_0} \end{array} \right]^T \Bigg|_{(\vec{x}^*, u^*)} \\ &= \left[\begin{array}{cc} \dfrac{\partial \left(\dfrac{r_{10} \sinh\left(\dfrac{r_{11} FV_1}{2R_G T} \right) + r_{12} I_0}{C_1} \right)}{\partial I_0} & \dfrac{\partial \left(\dfrac{r_{20} |V_2|^{1 - r_{21}} + r_{22} I_0}{C_2} \right)}{\partial I_0} \end{array} \right]^T \Bigg|_{(\vec{x}^*, u^*)} \\ &= \left[\begin{array}{cc} r_{12} / C_1 & r_{22} / C_2 \end{array} \right]^T \end{aligned} \tag{21}$$

And the final two Jacobians for the linearized output equation,

$$\vec{C} = \left.\frac{\partial g}{\partial \vec{x}}\right|_{(\vec{x}^*,\, u^*)} = \left.\begin{bmatrix} \frac{\partial (V_{term})}{\partial V_1} & \frac{\partial (V_{term})}{\partial V_2} \end{bmatrix}\right|_{(\vec{x}^*,\, u^*)}$$

$$= \left.\begin{bmatrix} \frac{\partial \left(V_{OCV} - V_0(I_0) - V_1 - V_2\right)}{\partial V_1} & \frac{\partial \left(V_{OCV} - V_0(I_0) - V_1 - V_2\right)}{\partial V_2} \end{bmatrix}\right|_{(\vec{x}^*,\, u^*)}$$

$$= \left.\begin{bmatrix} \frac{\partial \left(V_{OCV} - r_0 |I_0|^{1-r_1} - V_1 - V_2\right)}{\partial V_1} & \frac{\partial \left(V_{OCV} - r_0 |I_0|^{1-r_1} - V_1 - V_2\right)}{\partial V_2} \end{bmatrix}\right|_{(\vec{x}^*,\, u^*)}$$

$$= \begin{bmatrix} -1 & -1 \end{bmatrix}$$

(22)

$$D = \left.\frac{\partial g}{\partial u}\right|_{(\vec{x}^*,\, u^*)} = \left.\frac{\partial V_{term}}{\partial I_0}\right|_{(\vec{x}^*,\, u^*)}$$

$$= \left.\frac{\partial \left(V_{OCV} - V_0(I_0) - V_1 - V_2\right)}{\partial I_0}\right|_{(\vec{x}^*,\, u^*)}$$

$$= \left.\frac{\partial \left(V_{OCV} - r_0 |I_0|^{1-r_1} - V_1 - V_2\right)}{\partial I_0}\right|_{(\vec{x}^*,\, u^*)}$$

$$= \left(r_0 r_1 - r_0\right) \left.|I_0|^{-r_1}\right|_{(\vec{x}^*,\, u^*)}$$

$$= \left(r_0 r_1 - r_0\right) |I_0{}^*|^{-r_1} \qquad (23)$$

Note that the absolute value in equation 25 is handled in the same way as the absolute value in equation 22. Finally, we can express the complete linearized model in matrix form as:

$$\frac{\mathrm{d}(\Delta\vec{x})}{\mathrm{d}t} = \begin{bmatrix} \dfrac{r_{10} r_{11} F \cosh\left(\dfrac{r_{11} F V_1^*}{2R_G T}\right)}{2R_G T C_1} & 0 \\ 0 & \dfrac{(r_{20} - r_{21} r_{20}) \left|V_2^*\right|^{-r_{21}}}{C_2} \end{bmatrix} \begin{bmatrix} \Delta V_1 \\ \Delta V_2 \end{bmatrix} + \begin{bmatrix} r_{12}/C_1 \\ r_{22}/C_2 \end{bmatrix} \Delta I_0$$

$$\Delta y(t) = \begin{bmatrix} -1 & -1 \end{bmatrix} \begin{bmatrix} \Delta V_1 \\ \Delta V_2 \end{bmatrix} + \left(r_0 r_1 - r_0\right) \left|I_0^*\right|^{-r_1} \Delta I_0$$

And broken into a standard system of ordinary differential equations:

$$\frac{\mathrm{d}\left(\Delta V_1\right)}{\mathrm{d}t} = \frac{r_{10} r_{11} F \cosh\left(\dfrac{r_{11} F V_1^*}{2R_G T}\right)}{2R_G T C_1} \Delta V_1 + \frac{r_{12} \Delta I_0}{C_1} \tag{24}$$

$$\frac{\mathrm{d}\left(\Delta V_2\right)}{\mathrm{d}t} = \frac{(r_{20} - r_{21} r_{20}) \left|V_2^*\right|^{-r_{21}} \Delta V_2 + r_{22} \Delta I_0}{C_2} \tag{25}$$

$$\Delta V_{term} = -\Delta V_1 - \Delta V_2 - \left(r_0 r_1 - r_0\right) \left|I_0^*\right|^{-r_1} \Delta I_0 \tag{26}$$

Linearized Model Implementation

See Appendix D for a block diagram of the implemented MATLAB model.

Fitting the Linearized Model to Small Pulse Discharges

Every test of the linearized model was done about an operating point of 1A constant current. Each test starts by generating a ‘ground-truth’ voltage response with the nonlinear model to act as a substitute for actual experimental data to validate the behavior of the linearized model. This ground-truth voltage response is what the linearized model attempts to simulate. Each current profile fed into the nonlinear model is structured generally as: A 1A bias discharge current applied for 200 seconds, followed by a pulse discharge perturbation to this bias current for 10-30 seconds, and finally a 50 second period with the perturbation removed and only the bias current remaining. This setup allows the operating point to be approximately steady-state before the perturbation current is applied and allows for the model to return to steady state by the end of the

test. The current profiles used for testing the linearized model are all generated artificially (in Microsoft Excel) as the NASA dataset used for fitting the nonlinear model contains no suitable data for testing perturbations about an operating point. Due to the previously established sensitivity of the nonlinear model to discharge current magnitude, only pulse discharges that have been previously verified on the nonlinear model using the NASA dataset can be trusted as accurate. These verified pulse discharges being: 1A, 1.5A, and 2.25A. It must be assumed that all other perturbation magnitudes may produce inaccurate voltage responses using the nonlinear model and therefore cannot be used to validate the linearized model.

To first verify the structure of the linearized model and to rule out any obvious errors, it was tested with a 10 second long 0.5A discharge pulse as the perturbation to the operating point. This was selected because it isn't a large enough or long enough perturbation to change V_{ocv} significantly, thus safely staying within the range of a linear voltage response. Figure 38 shows the current profile applied to the nonlinear model used to generate the ground-truth voltage response (figure 39) that is used in place of experimental data by the linearized model. The nonlinear model was using the parameters which resulted in the best 1A pulse discharge fit (figure 26) when generating this voltage response.

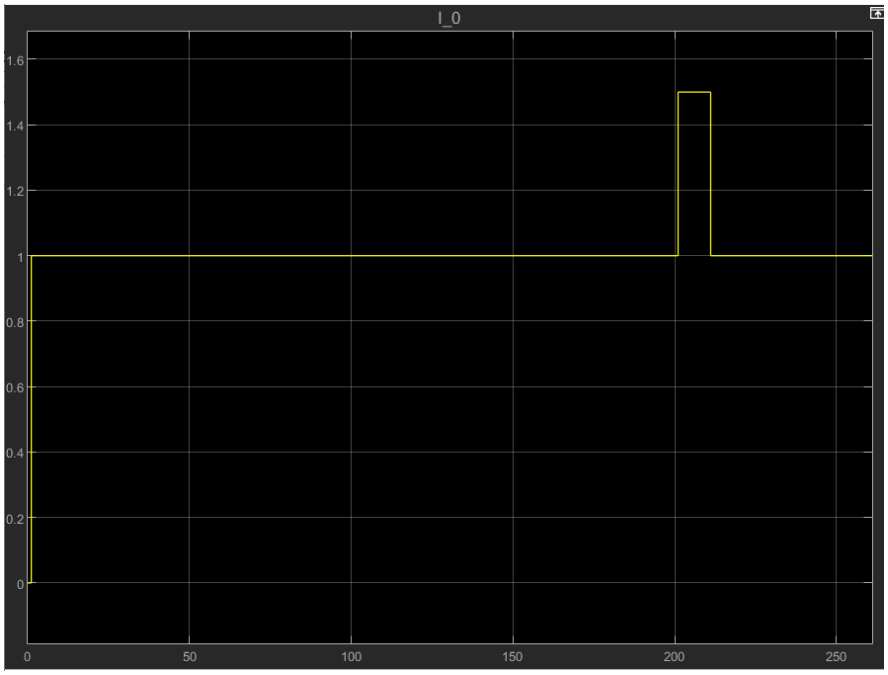

Figure 38: Current profile applied to the nonlinear model used to generate the ground-truth voltage response for use by the linearized model.

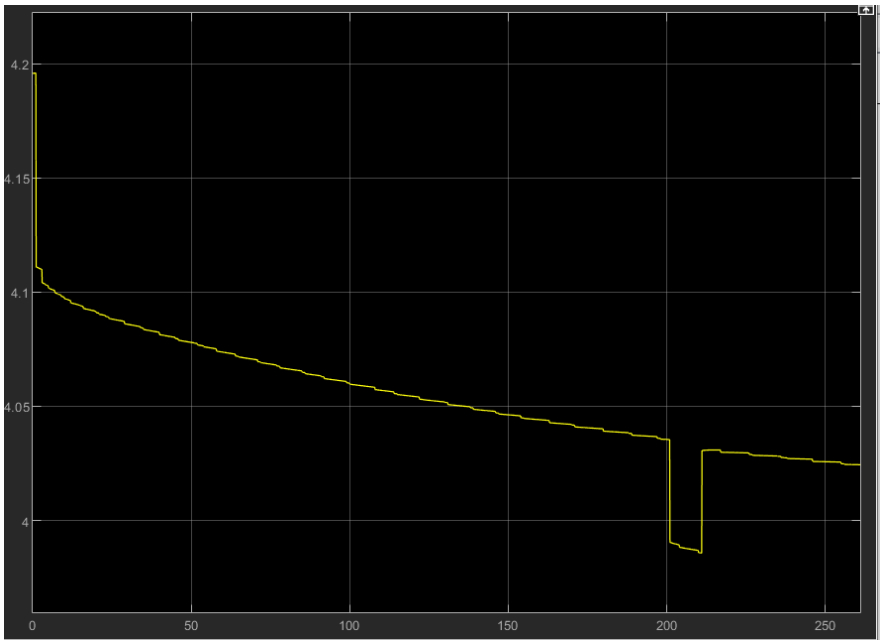

Figure 39: Voltage response generated by the nonlinear model when stimulated by the current profile shown in figure 38.

This current profile and voltage response were then passed into the linearized model, and an optimization process was carried out using Simulink's nonlinear least squares routine. The resulting voltage response output by the optimized linearized model is shown in figure 40. Note that the variable being optimized over is ΔV_{term} , so the voltage response is with respect to the 1A operating point.

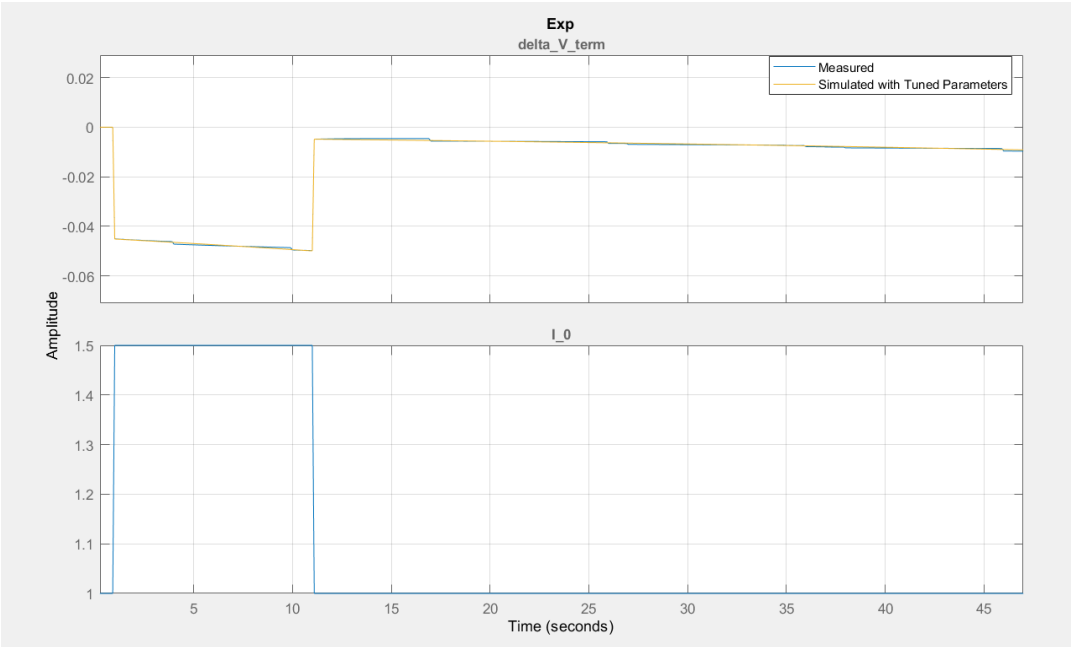

Figure 40: Voltage response of the linearized model as fit to a 10-second, 0.5A perturbation away from the operating point.

Seeing as the voltage response matches nearly identically using a 0.5A perturbation, the next step is to incrementally push the magnitude of the perturbation higher until the linearized model begins to fail to reproduce the voltage response generated by the nonlinear model.

Investigating the Pulse Discharge Magnitude Limitations of the Linearized Model

The first step up in perturbation magnitude was a 1A pulse discharge applied for 10 seconds. The linearized model produces a near identical response to the nonlinear model after its parameters were optimized using Simulink's nonlinear least squares routine. The nonlinear model was still using the parameters which resulted in the best 1A pulse discharge fit (figure 26) when generating this voltage response. Figure 41 shows the linearized and nonlinear voltage responses overlaid.

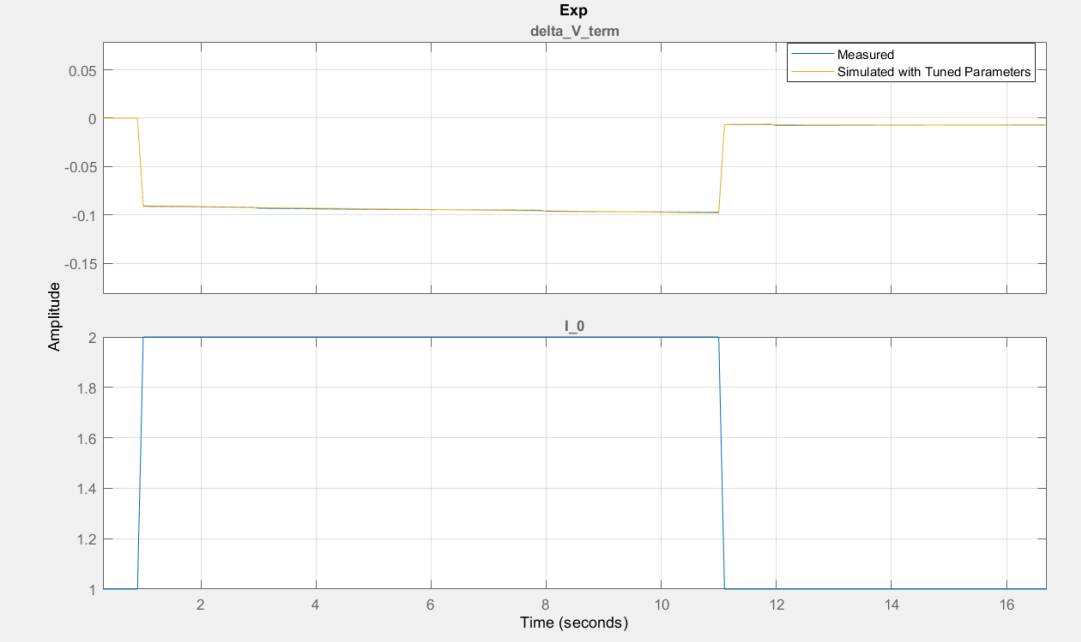

Figure 41: Voltage response of the linearized model as fit to a 10-second, 1A perturbation away from the operating point.

```
% Operating Point Parameters
I_0_star = 1;
V_1_star = 0.040467936428451;
V_2_star = -0.001962421978295;
```

Figure 42: Operating point at which the linearized model was evaluated for the test shown in figure 41.

The next step up in perturbation magnitude was a 1.5A pulse discharge applied for 10 seconds. The linearized model produces a near identical response to the nonlinear model again. The nonlinear model was using the parameters which resulted in the best 1.5A pulse discharge fit (figure 30) when generating the ground-truth voltage response. Figure 43 shows the linearized and nonlinear voltage responses overlaid. Figure 44 shows the corresponding residuals for this voltage response. Figure 45 shows the operating point at which the test was done.

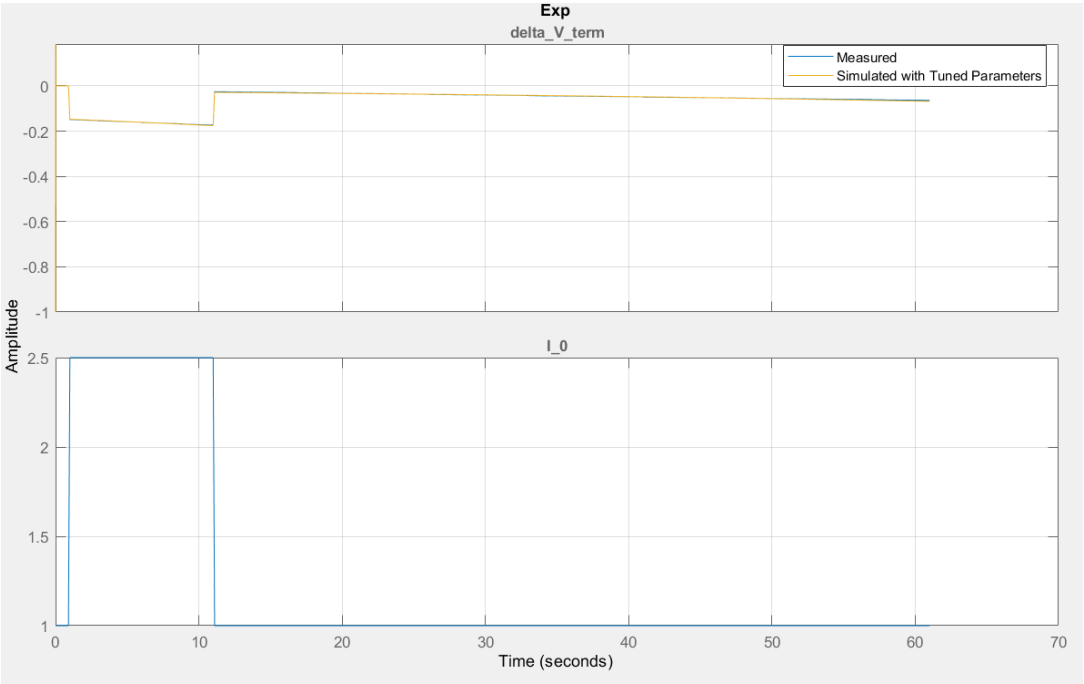

Figure 43: Voltage response of the linearized model as fit to a 10-second, 1.5A perturbation away from the operating point.

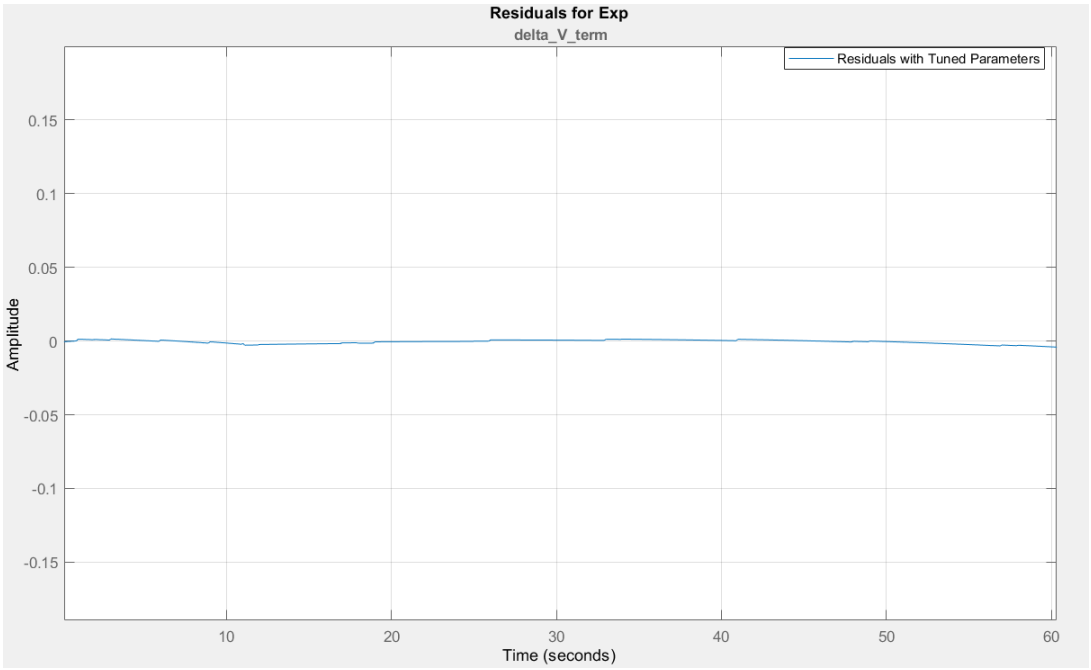

Figure 44: Residuals from the voltage response of the linearized model shown in figure 43.

```
% Operating Point Parameters
I_0_star = 1;
V_1_star = 0.071912763599044;
V_2_star = 0.088614937530378;
```

Figure 45: Operating point at which the linearized model was evaluated for the test shown in figure 43.

The next step up in perturbation magnitude was a 2.25A pulse discharge applied for 10 seconds. Here the linearized model response begins to deviate from the nonlinear model response. The nonlinear model was using the parameters which resulted in the best 2.25A pulse discharge fit (figure 34) when generating this voltage response. Figure 46 shows the linearized and nonlinear voltage responses overlaid. Figure 47 shows the corresponding residuals for this voltage response. Figure 48 shows the operating point at which the test was done.

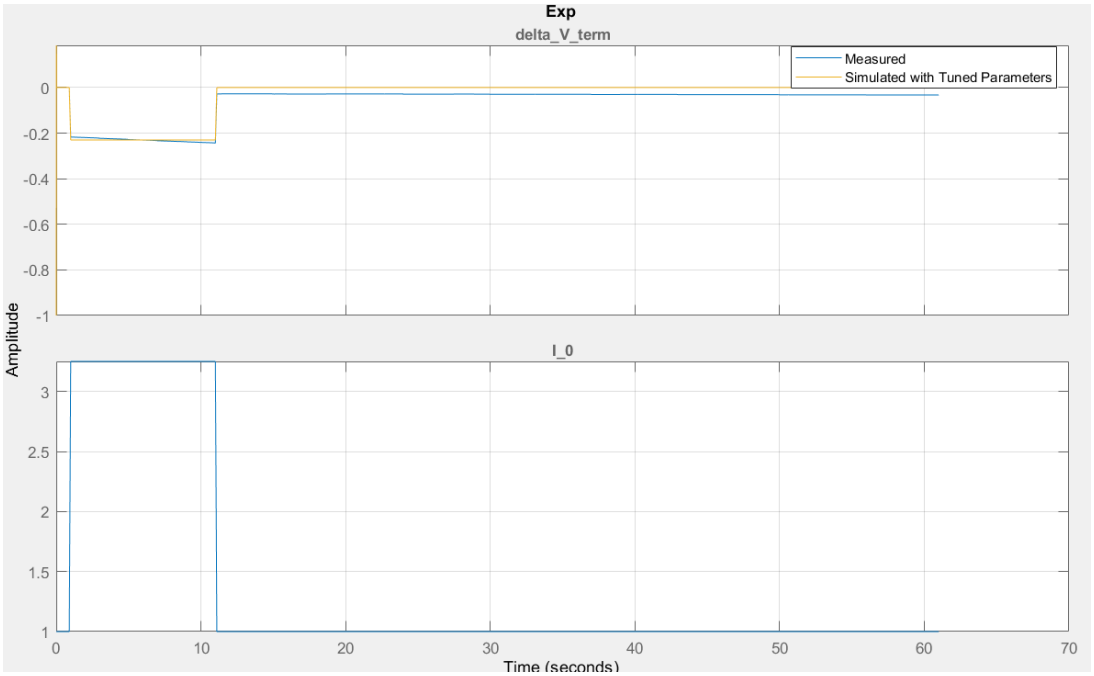

Figure 46: Voltage response of the linearized model as fit to a 10-second, 2.25A perturbation away from the operating point.

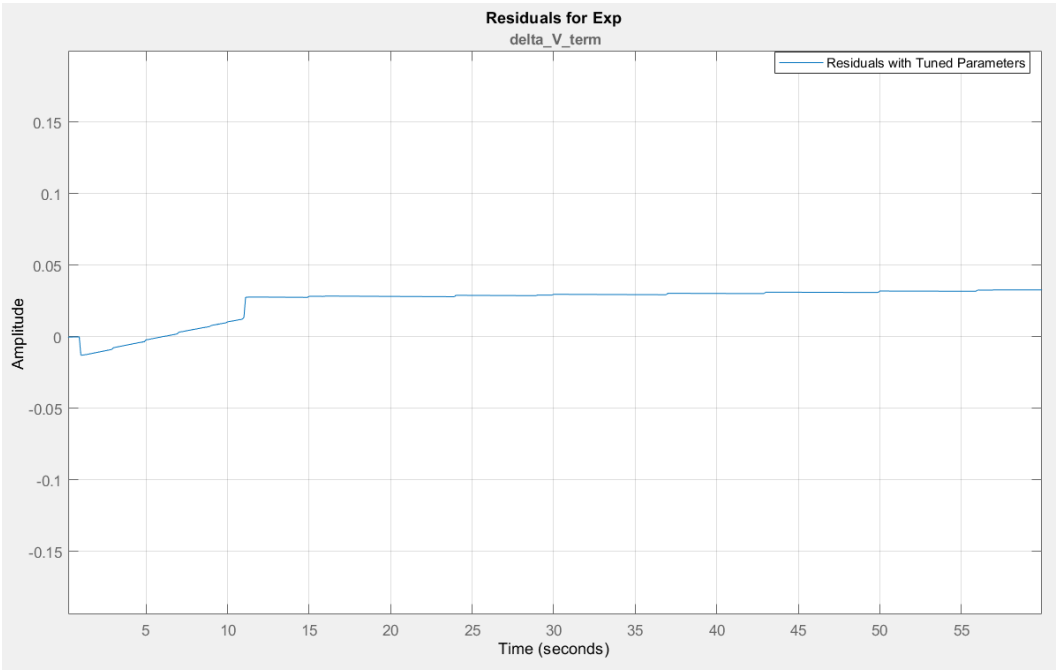

Figure 47: Residuals from the voltage response of the linearized model shown in figure 46.

```
% Operating Point Parameters
I_0_star = 1;
V_1_star = 0.076655090373554;
V_2_star = 0.048821848903553;
```

Figure 48: Operating point at which the linearized model was evaluated for the test shown in figure 46.

These results suggest that the linearized model is viable for simulating voltage responses of up to 2.25A for a maximum of 10 seconds at an operating point of 1A DC current.

Investigating the Pulse Discharge Duration Limitations of the Linearized Model

Now that the nonlinear model has been pushed to the highest pulse discharge current it has been verifiably able to simulate and the linearized model is still keeping up relatively well, the *duration* of the discharge pulse is the other parameter we can play with to investigate the limits of the linearized model. The parameters in the linearized model, as optimized using the 10 second perturbation data, are kept the same through these extended duration tests.

First, using a 1A perturbation away from the operating point, the perturbation duration is increased in increments of 10 seconds. Figure 49 shows the linearized model response to a 20 second, 1A pulse discharge perturbation. Figure 50 shows the linearized model response to a 30 second, 1A pulse discharge perturbation. Figure 51 shows the residuals corresponding to the response in figure 50.

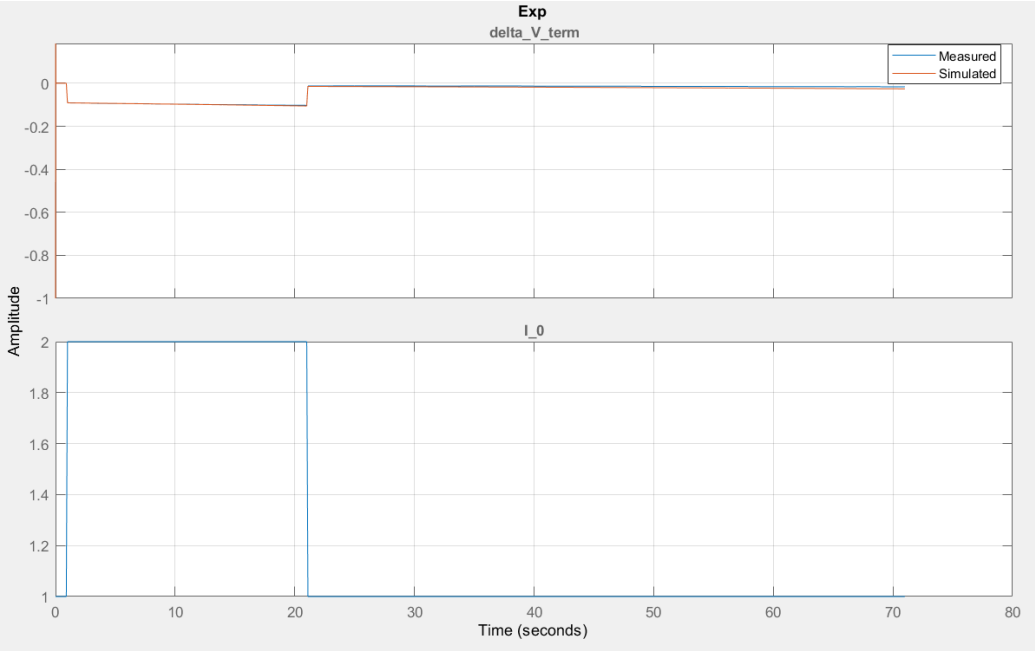

Figure 49: Linearized model response to 20 second, 1A pulse discharge perturbation away from the operating point.

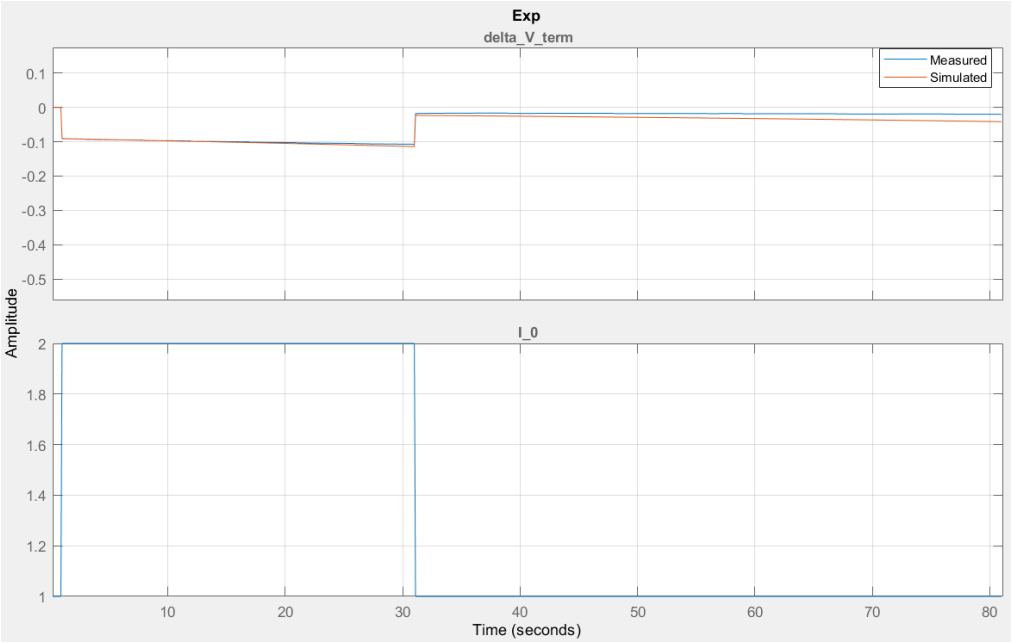

Figure 50: Linearized model response to 30 second, 1A pulse discharge perturbation away from the operating point.

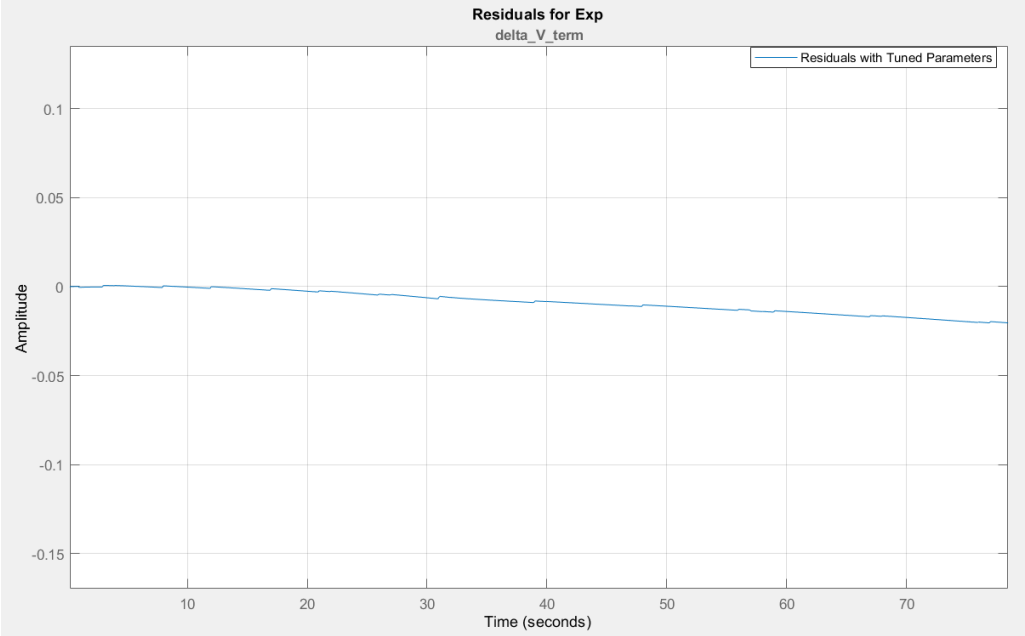

Figure 51: Residuals from the linearized model response shown in figure 50.

Figure 51 illustrates the deviation of the linearized model response as the duration exceeds 20 seconds.

Next, using a 1.5A perturbation away from the operating point, the perturbation duration is increased in increments of 10 seconds. Figure 52 shows the linearized model response to a 20 second pulse discharge perturbation. Figure 53 shows the residuals corresponding to the response in figure 49. Figure 54 shows the linearized model response to a 30 second pulse discharge perturbation. Figure 55 shows the residuals corresponding to the response in figure 54.

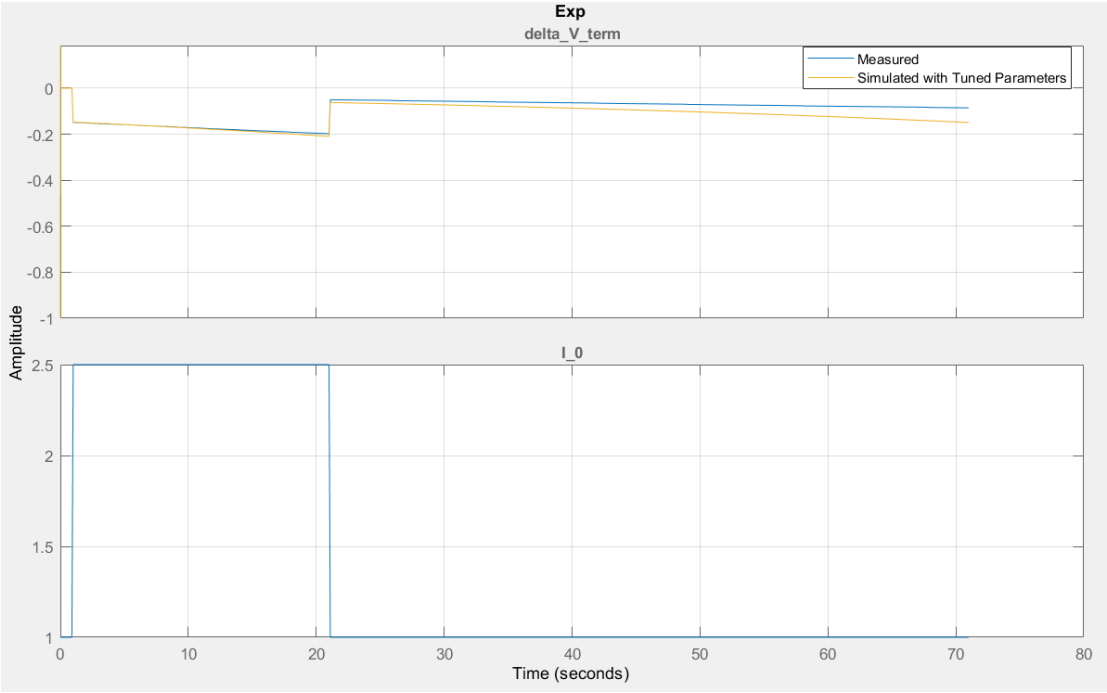

Figure 52: Linearized model response to 20 second, 1.5A pulse discharge perturbation away from the operating point.

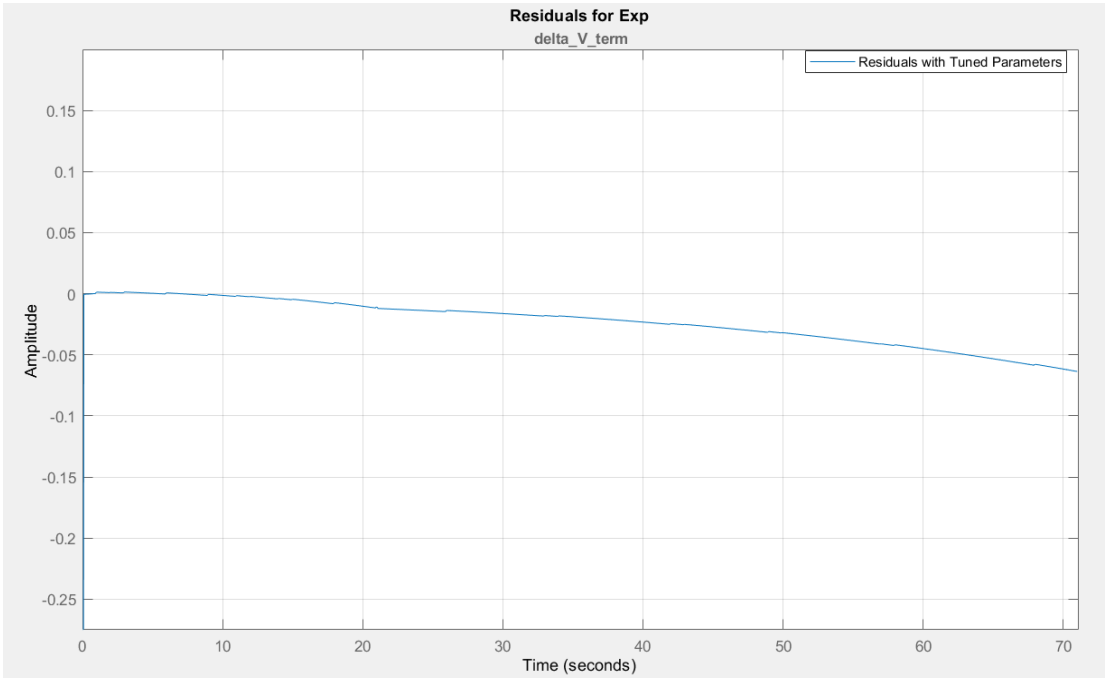

Figure 53: Residuals from the linearized model response shown in figure 52.

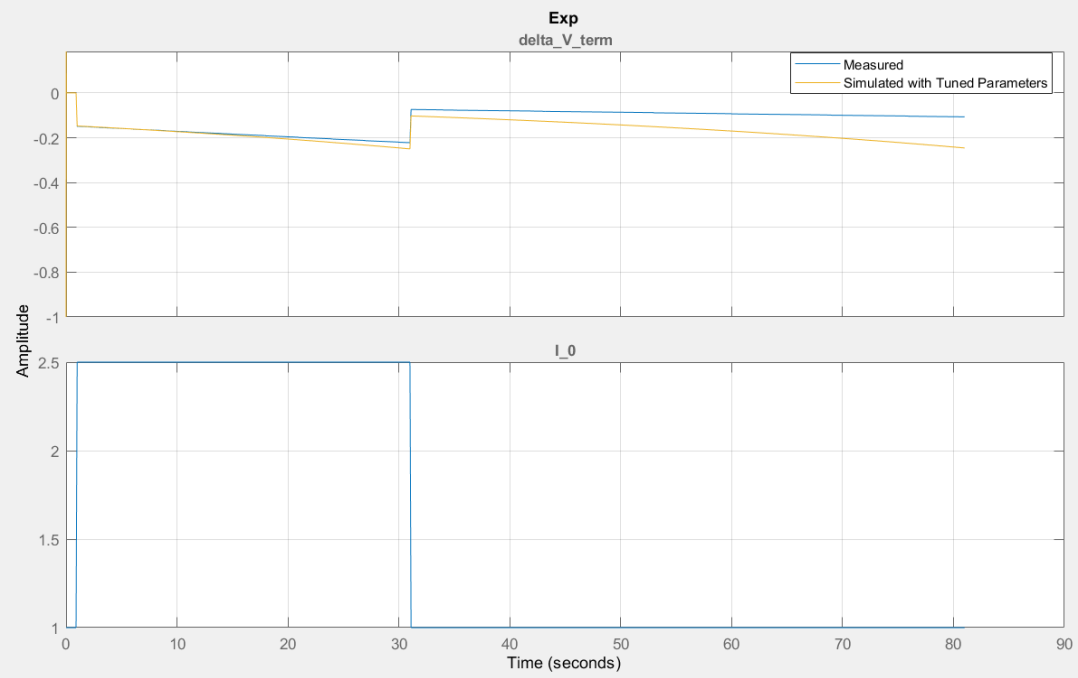

Figure 54: Linearized model response to 30 second, 1.5A pulse discharge perturbation away from the operating point.

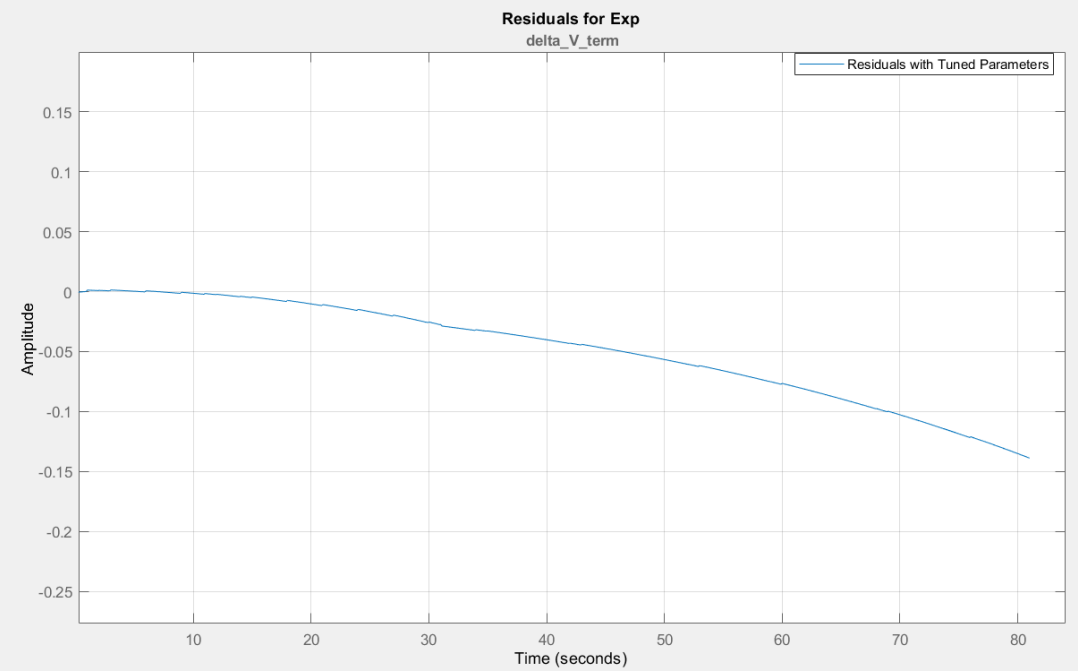

Figure 55: Residuals from the linearized model response shown in figure 54.

These tests show that the higher magnitude perturbation causes the linearized model response to deviate more quickly from nonlinear model response.

Finally, using a 2.25A perturbation away from the operating point, the perturbation duration is increased in increments of 10 seconds. Figure 56 shows the linearized model response to a 20 second pulse discharge perturbation. Figure 57 shows the residuals corresponding to the response in figure 56. Figure 58 shows the linearized model response to a 30 second pulse discharge perturbation. Figure 59 shows the residuals corresponding to the response in figure 58.

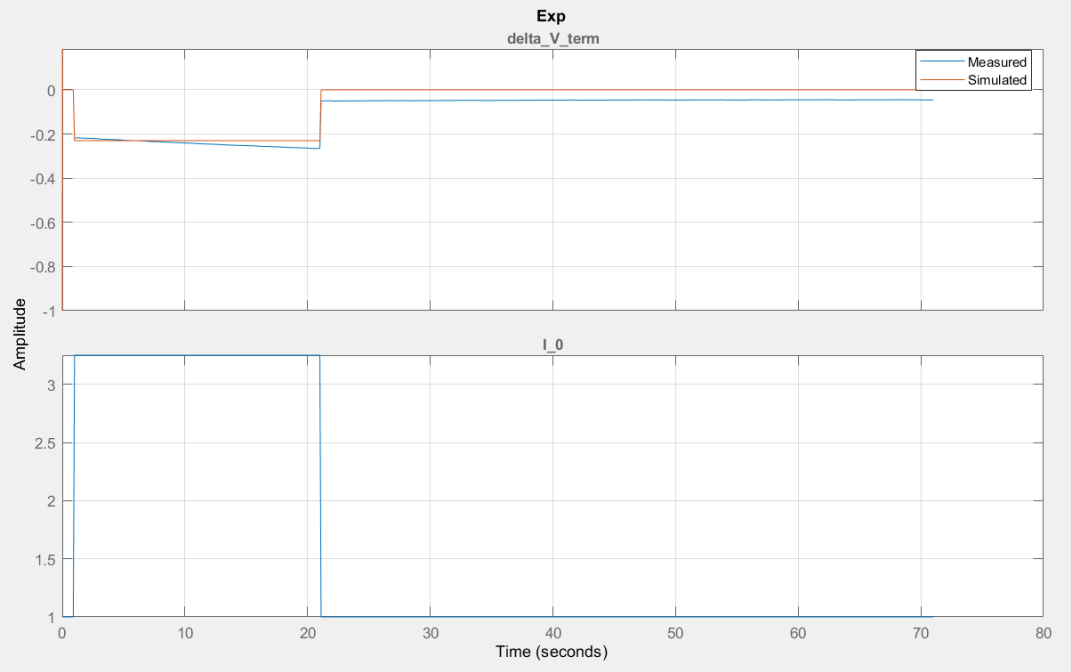

Figure 56: Linearized model response to 20 second, 2.25A pulse discharge perturbation away from the operating point.

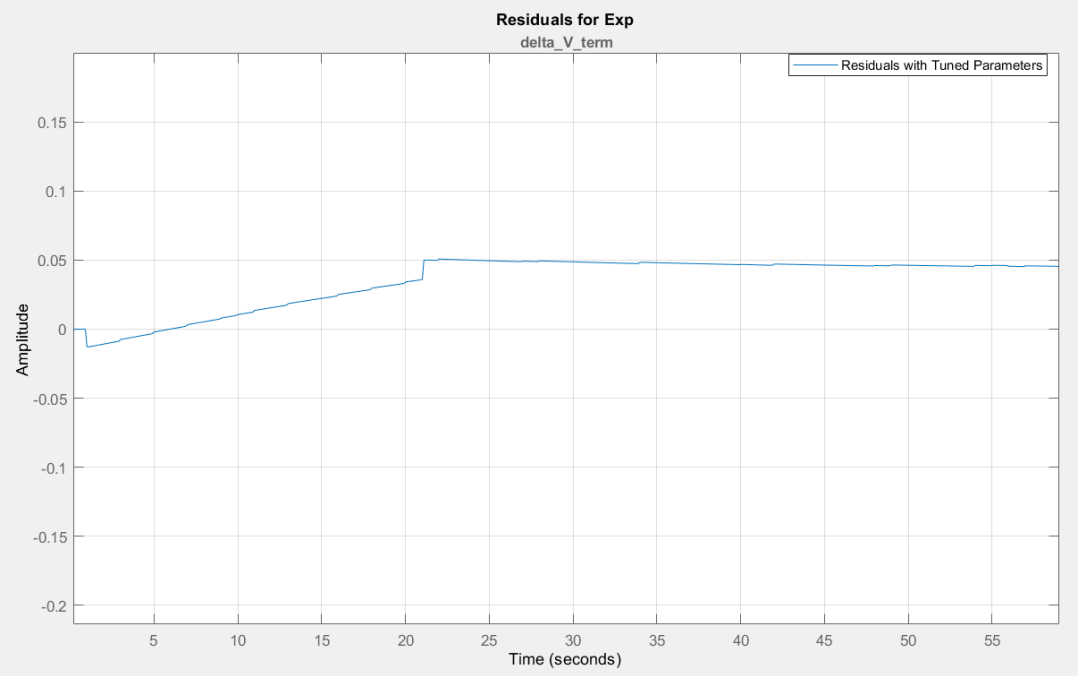

Figure 57: Residuals from the linearized model response shown in figure 56.

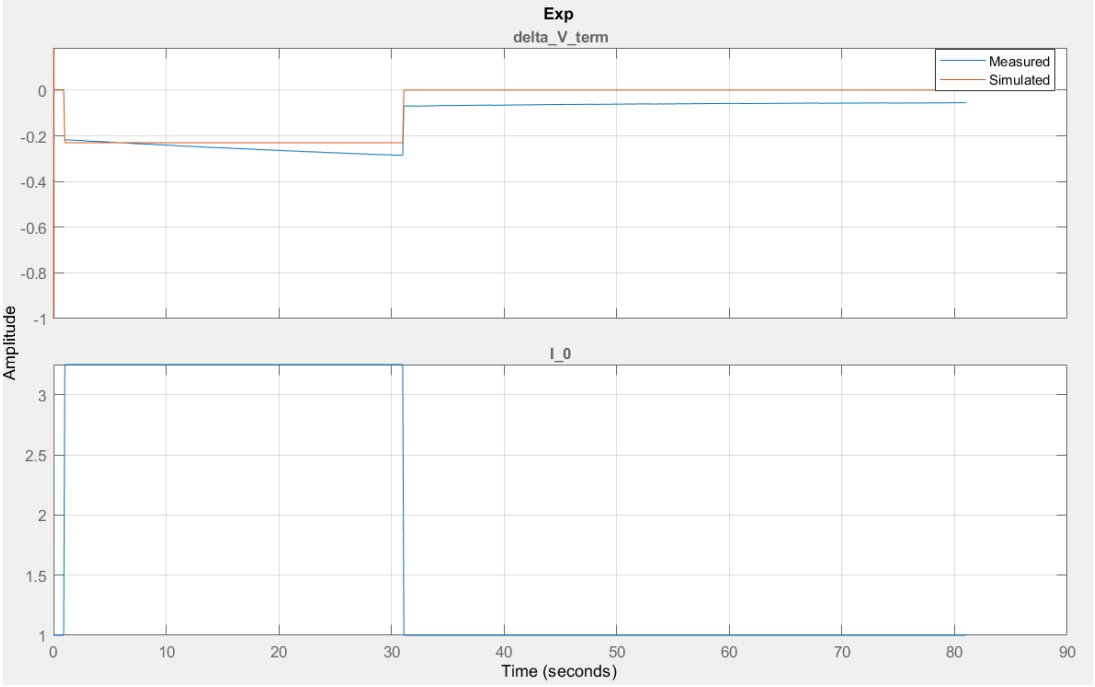

Figure 58: Linearized model response to 30 second, 2.25A pulse discharge perturbation away from the operating point.

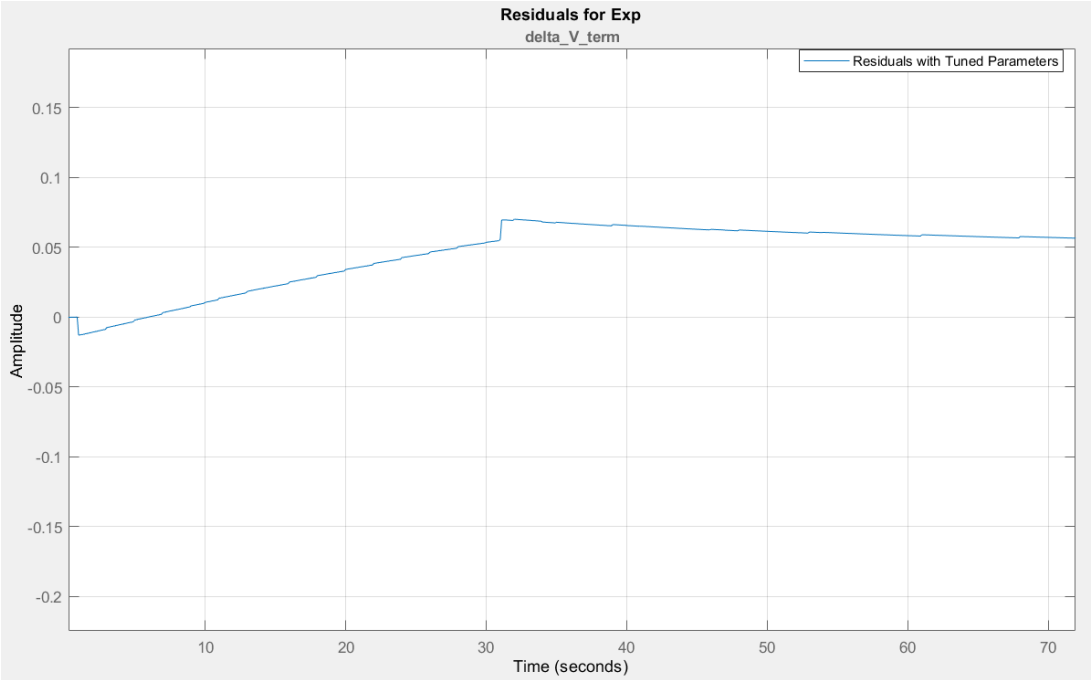

Figure 59: Residuals from the linearized model response shown in figure 58.

Again, it is clear from these tests that higher magnitude perturbations cause the linearized model response to deviate more quickly from nonlinear model response as compared to smaller magnitude perturbations.

Conclusion

This thesis investigates the ability of two battery models to accurately simulate the terminal voltage of a lithium-ion cell with the higher level goal of improving energy management algorithms in electric vehicles.

A nonlinear model is developed and tested, yielding a voltage response with less than 4 millivolts of error compared to the experimental voltage response in the region of interest for direct current resistance estimation. The interpretability of the model is promising in some aspects, offering insights into the charge transfer reaction of the battery it models, but offering few insights into other processes occurring in the battery. The generalizability of this model is found to be questionable at best for reasons that require further investigation. The importance of initializing model parameter values such that they start near a global minimum is highlighted when the nonlinear model is fit to pulse discharges >1A as its parameter values change drastically, yet the overall behavior of the model is relatively unchanged.

A linearized version of the nonlinear model is developed and tested, revealing its potential to be a simpler, but still effective alternative to the nonlinear model for predicting voltage response around specific operating points. The results of the tests on the linearized model must still be questioned as they were validated against data generated by the nonlinear model, which has its previously established generalizability and parameter instability issues.

While energy management algorithms will not likely be improved directly using the results in this thesis, the work presented here adds to the existing literature by thoroughly documenting the battery model development and testing process, at the level of undergraduate research, such that others new to the field can learn and build upon the successes and failures of this work.

Future Work

The models and simulation results presented in this thesis provide a solid basis for further investigation. The following avenues for future work are each potentially fruitful in the pursuit of more accurate, generalizable, and stable models:

- Determining a robust method for initializing both nonlinear and linearized model parameter values such that they start as close to a global minimum as possible. This could reduce the computation time required for parameter estimation and could result in more accurate and generalizable models.

- Add model components derived directly from physical processes for the electrode and electrolyte resistances, the solid-state diffusion process, or both. This could improve the interpretability of the models, the extensibility of the models, or both.

- Evaluate the effects of using different parameter estimation routines on both final model performance and parameter estimation time.

Appendix A: Battery Pack Architecture

Figure A1 shows how individual lithium-ion cells may be assembled into a battery pack to increase the total pack voltage and to increase the maximum current rating. The shown configuration consists of 4 cells in parallel, creating 3 parallel modules, which are then wired in series, creating a 4-parallel-3-series battery pack configuration. This pack therefore has an effective voltage of 3x the individual cell voltages, and a maximum current rating of 4x the current rating of the individual cells, as specified in the cell manufacturer's datasheet.

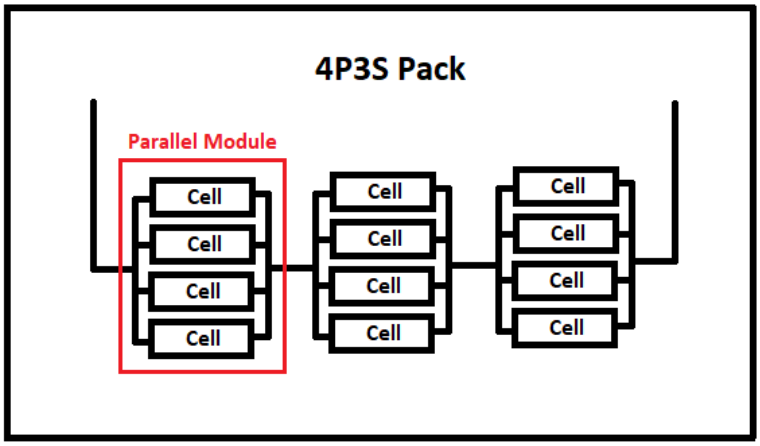

Figure A1: A potential battery pack configuration with 4 lithium-ion cells in parallel, forming a parallel module, and 3 of these parallel modules in series (4P3S).

Appendix B: Electrochemical Impedance Spectroscopy

Electrochemical impedance spectroscopy (EIS) is a method commonly used in the laboratory for determining battery impedance characteristics with a high level of accuracy based on frequency-domain measurements. Typically, a small sinusoidal voltage (or current) is imposed across a battery that was previously in a steady state, and the resulting current (or voltage) response is measured. The frequency of this imposed voltage signal is varied across a broad range (1 Hz - 10000 Hz for example) to get a full characterization of the battery impedance. The amplitude of the imposed voltage must be small enough to keep the current response pseudo-linear but large enough to achieve a signal-to-noise ratio that enables effective current response measurements. If the imposed voltage signal is too large, the current response will contain harmonics of the excitation frequency, complicating the resulting data [27]. One standard way of analyzing the generated EIS data is to fit the parameters of a small-signal battery model to the EIS data using any suitable nonlinear curve-fitting technique, such as nonlinear least squares. The resulting model, now populated with values based on empirical data, represents the impedance characteristics of the battery under test.

The primary downside of these methods is that they require specialized circuits for active signal generation to be built into the BMS, incurring additional manufacturing costs [28]. To avoid these additional circuits, passive impedance spectroscopy techniques have been developed in [29] [30]. These methods propose using the current fluctuations caused by natural loading of the battery to do EIS measurements. The issue is that these fluctuations must be periodic, of a suitable amplitude to preserve linearity in the current response, and in a frequency range useful for the calculation of battery impedance. These conditions may not be fulfilled by a particular application.

Appendix C: Simulink Implementation of the Nonlinear Battery Model

$$dV_1/dt = \frac{r_{10}\sinh(r_{11}\eta) + r_{12}I_0}{C_1} \quad (14)$$

$$dV_2/dt = \frac{r_{20}|V_2|^{1-r_{21}} + r_{22}I_0}{C_2} \quad (15)$$

$$V_{term} = V_{OCV} - r_0|I_0|^{1-r_1} - V_1 - V_2 \quad (16)$$

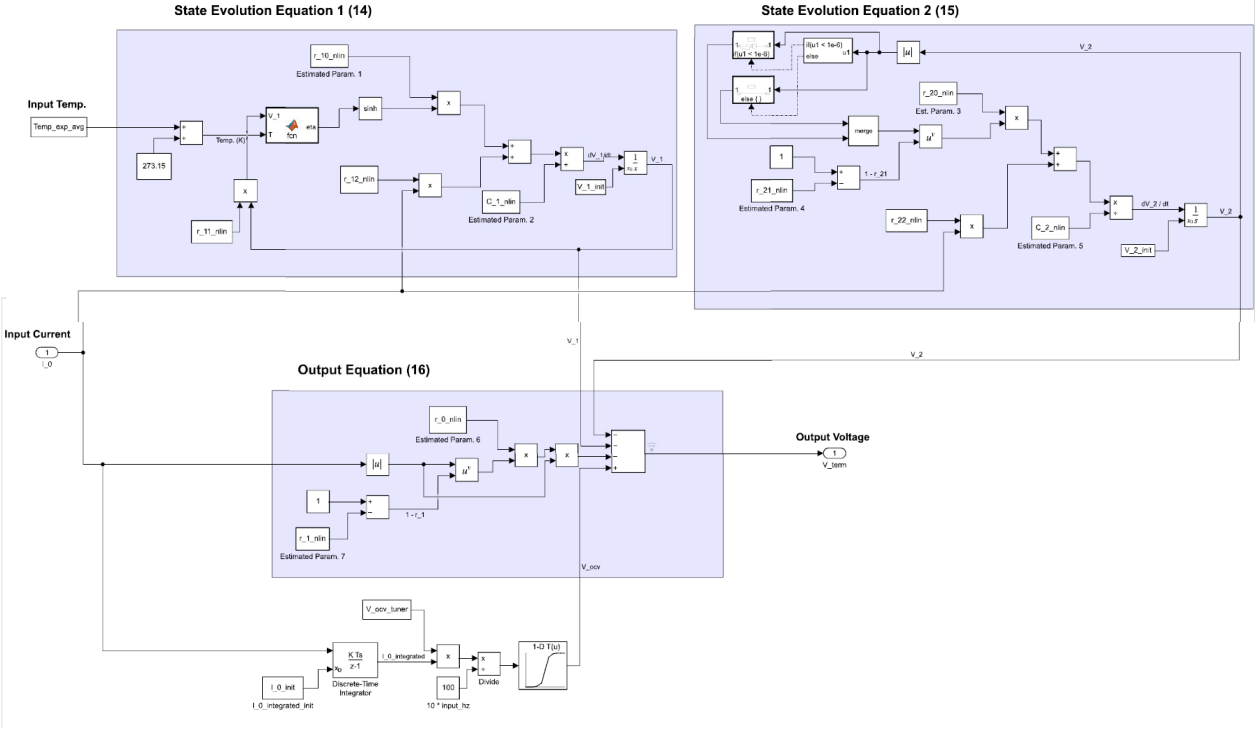

Appendix D: Simulink Implementation of the Linearized Battery Model

$$\frac{\mathrm{d}\left(\Delta V_1\right)}{\mathrm{d}t} = \frac{r_{10} r_{11} F \cosh\left(\frac{r_{11} F V_1^{*}}{2 R_G T}\right)}{2 R_G T C_1} \Delta V_1 + \frac{r_{12} \Delta I_0}{C_1} \tag{24}$$

$$\frac{\mathrm{d}\left(\Delta V_2\right)}{\mathrm{d}t} = \frac{\left(r_{20} - r_{21} r_{20}\right) \left|V_2^{*}\right|^{-r_{21}} \Delta V_2 + r_{22} \Delta I_0}{C_2} \tag{25}$$

$$\Delta V_{term} = -\Delta V_1 - \Delta V_2 - \left(r_0 r_1 - r_0\right) \left|I_0^{*}\right|^{-r_1} \Delta I_0 \tag{26}$$

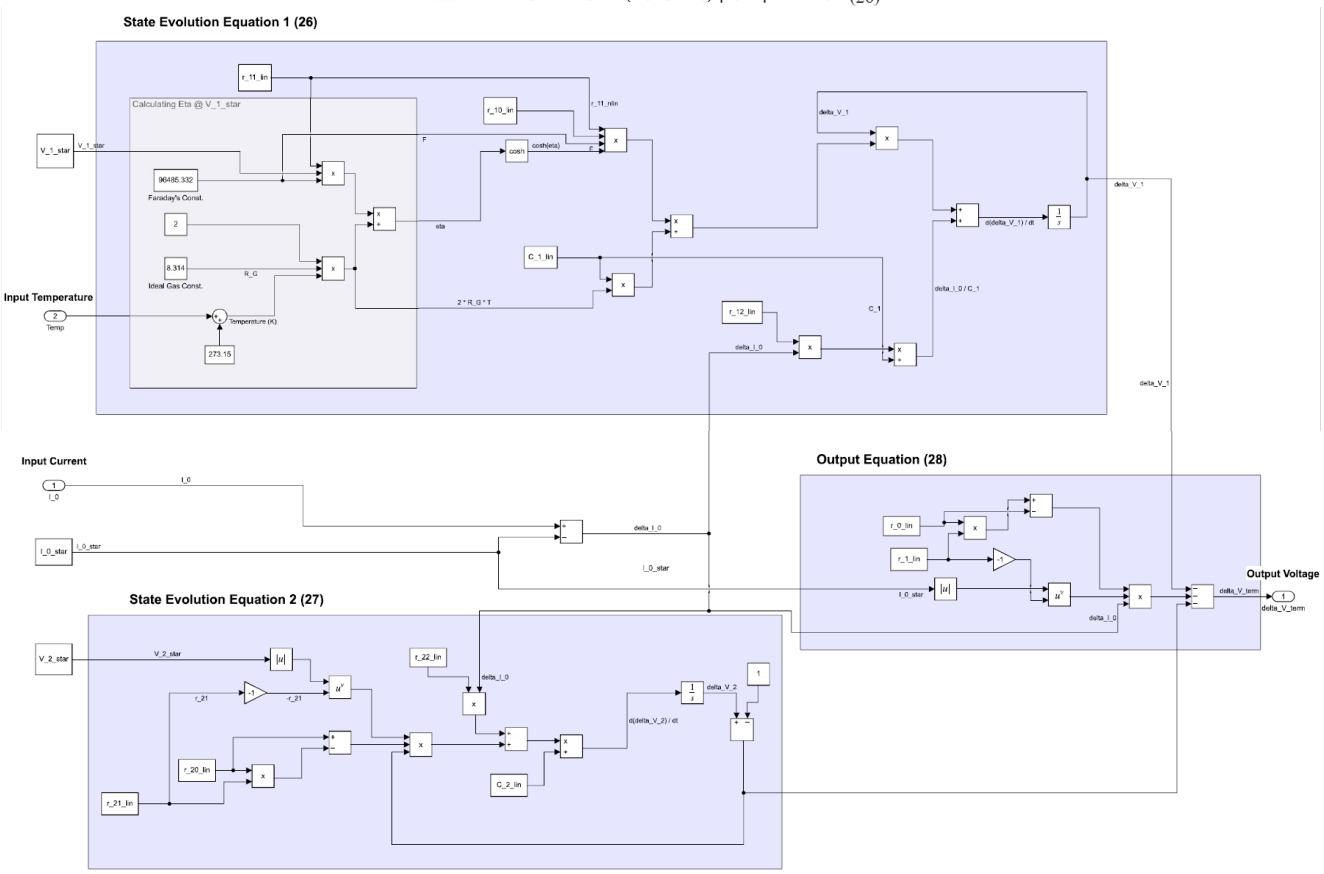

References

[1] A. Smorodin, “2021: Another chapter in the global race towards electrification,” *International Council on Clean Transportation*, Mar. 04, 2022. [Online]. Available: https://theicct.org/2021-global-race-evs-mar22/. [Accessed: Apr. 09, 2023]

[2] L. Paoli, “Electric Vehicles,” *IEA*. [Online]. Available: https://www.iea.org/reports/electric-vehicles. [Accessed: Apr. 09, 2023]

[3] “Electric vs. Gas Cars: Is It Cheaper to Drive an EV?” [Online]. Available: https://www.nrdc.org/stories/electric-vs-gas-it-cheaper-drive-ev. [Accessed: Apr. 09, 2023]

[4] A. Lougovoy, “Identifying Critical Steps Towards Electric Vehicle Mass Adoption,” *Vulog*, Jan. 25, 2019. [Online]. Available: https://www.vulog.com/blog/accelerating-electrification-the-move-towards-ev-mass-adoption/. [Accessed: Apr. 09, 2023]

[5] A. König, L. Nicoletti, D. Schröder, S. Wolff, A. Waclaw, and M. Lienkamp, “An Overview of Parameter and Cost for Battery Electric Vehicles,” *World Electric Vehicle Journal*, vol. 12, no. 1, p. 21, Feb. 2021, doi: 10.3390/wevj12010021. [Online]. Available: https://www.mdpi.com/2032-6653/12/1/21. [Accessed: Apr. 09, 2023]

[6] “Breaking down the cost of an EV battery cell,” *Mining.com*. [Online]. Available: https://www.mining.com/web/breaking-down-the-cost-of-an-ev-battery-cell/

[7] W. Waag, S. Käbitz, and D. U. Sauer, “Experimental investigation of the lithium-ion battery impedance characteristic at various conditions and aging states and its influence on the application,” *Appl. Energy*, vol. 102, pp. 885–897, Feb. 2013, doi: 10.1016/j.apenergy.2012.09.030. [Online]. Available: https://www.sciencedirect.com/science/article/pii/S030626191200671X

[8] G. L. Plett, “High-performance battery-pack power estimation using a dynamic cell model,” *IEEE Trans. Veh. Technol.*, vol. 53, no. 5, pp. 1586–1593, Sep. 2004, doi: 10.1109/TVT.2004.832408. [Online]. Available: http://dx.doi.org/10.1109/TVT.2004.832408

[9] S. Wang, M. Verbrugge, J. S. Wang, and P. Liu, “Power prediction from a battery state estimator that incorporates diffusion resistance,” *J. Power Sources*, vol. 214, pp. 399–406, Sep. 2012, doi: 10.1016/j.jpowsour.2012.04.070. [Online]. Available: https://www.sciencedirect.com/science/article/pii/S037877531200804X

[10] Y. Preger, L. Torres-Castro, J. McDowall, and Others, “Lithium-ion Batteries,” *2020 USDOE Energy Storage Handbook* [Online]. Available: https://www.sandia.gov/ess-ssl/wp-content/uploads/2021/03/ESHB-Ch3_Lithium-Batteries_Preger.pdf

[11] S. Hemavathi, “Overview of cell balancing methods for Li-ion battery technology,” *Wiley Online Library*. [Online]. Available: https://onlinelibrary.wiley.com/doi/full/10.1002/est2.203. [Accessed: Apr. 09, 2023]

[12] “Novel Energy Management Strategy for Electric Vehicles to Improve Driving Range.” [Online]. Available: https://ieeexplore.ieee.org/document/9915445. [Accessed: Apr. 09, 2023]

[13] “BU-1003a: Battery aging in an electric vehicle (EV),” *Battery University*, Sep. 07, 2010. [Online]. Available: https://batteryuniversity.com/article/bu-1003a-battery-aging-in-an-electric-vehicle-ev. [Accessed: Apr. 09, 2023]

[14] “Charging Your Lithium Battery Below Zero,” *DC Battery Technologies*, Jan. 25, 2021. [Online]. Available: https://dcbattery.tech/charging_your_lithium_battery_below_zero/. [Accessed: Apr. 09, 2023]

[15] S. Ma *et al.*, “Temperature effect and thermal impact in lithium-ion batteries: A review,” *Progress in Natural Science: Materials International*, vol. 28, no. 6, pp. 653–666, Dec. 2018, doi: 10.1016/j.pnsc.2018.11.002. [Online]. Available: https://www.sciencedirect.com/science/article/pii/S1002007118307536

[16] “Battery Management System.” [Online]. Available: https://www.xaltenergy.com/portfolio/battery-management-system-bms/. [Accessed: Apr. 10, 2023]

[17] “Introduction to Battery Management Part 3 - TI.” [Online]. Available: https://www.digikey.at/de/ptm/t/texas-instruments/introduction-to-battery-management-part-3/tutorial?_ga=2.46749607.165133155.1682019831-969174754.1682019830. [Accessed: Apr. 20, 2023]

[18] Y. Li and Y. Qi, “Energy landscape of the charge transfer reaction at the complex Li/SEI/electrolyte interface,” *Energy Environ. Sci.*, vol. 12, no. 4, pp. 1286–1295, Apr. 2019, doi: 10.1039/C8EE03586E. [Online]. Available: https://pubs.rsc.org/en/content/articlelanding/2019/ee/c8ee03586e. [Accessed: Apr. 09, 2023]

[19] C. M. Julien and M. Massot, “Raman spectroscopic studies of lithium manganates with spinel structure,” *J. Phys. Condens. Matter*, vol. 15, no. 19, p. 3151, May 2003, doi: 10.1088/0953-8984/15/19/315. [Online]. Available: https://iopscience.iop.org/article/10.1088/0953-8984/15/19/315/meta. [Accessed: Apr. 09, 2023]

[20] M. Doyle, J. Newman, A. S. Gozdz, C. N. Schmutz, and J. Tarascon, “Comparison of Modeling Predictions with Experimental Data from Plastic Lithium Ion Cells,” *J. Electrochem. Soc.*, vol. 143, no. 6, p. 1890, Jun. 1996, doi: 10.1149/1.1836921. [Online]. Available: https://iopscience.iop.org/article/10.1149/1.1836921/meta. [Accessed: Apr. 09, 2023]

[21] F. J. Günter, C. Burgstaller, F. Konwitschny, and G. Reinhart, “Influence of the electrolyte quantity on lithium-ion cells,” *J. Electrochem. Soc.*, vol. 166, no. 10, pp. A1709–A1714, 2019, doi: 10.1149/2.0121910jes. [Online]. Available: https://iopscience.iop.org/article/10.1149/2.0121910jes

[22] J. S. Edge *et al.*, “Lithium ion battery degradation: what you need to know,” *Phys. Chem.*

Chem. Phys., vol. 23, no. 14, pp. 8200–8221, Apr. 2021, doi: 10.1039/d1cp00359c. [Online]. Available: http://dx.doi.org/10.1039/d1cp00359c

[23] T. R. Jow, S. A. Delp, J. L. Allen, J.-P. Jones, and M. C. Smart, “Factors limiting Li+charge transfer kinetics in Li-ion batteries,” *J. Electrochem. Soc.*, vol. 165, no. 2, pp. A361–A367, 2018, doi: 10.1149/2.1221802jes. [Online]. Available: https://iopscience.iop.org/article/10.1149/2.1221802jes

[24] W. Waag, C. Fleischer, and D. U. Sauer, “Critical review of the methods for monitoring of lithium-ion batteries in electric and hybrid vehicles,” *J. Power Sources*, vol. 258, pp. 321–339, Jul. 2014, doi: 10.1016/j.jpowsour.2014.02.064. [Online]. Available: https://www.sciencedirect.com/science/article/pii/S0378775314002572

[25] K. S. Hariharan and V. Senthil Kumar, “A nonlinear equivalent circuit model for lithium ion cells,” *J. Power Sources*, vol. 222, pp. 210–217, Jan. 2013, doi: 10.1016/j.jpowsour.2012.08.090. [Online]. Available: https://www.sciencedirect.com/science/article/pii/S0378775312013973

[26] “Randomized battery usage 1: Random walk,” *NASA*. [Online]. Available: https://data.nasa.gov/Raw-Data/Randomized-Battery-Usage-1-Random-Walk/ugxu-9kjx/data. [Accessed: Apr. 10, 2023]

[27] “Basics of EIS: Electrochemical Research-impedance Gamry instruments.” [Online]. Available: https://www.gamry.com/application-notes/EIS/basics-of-electrochemical-impedance-spectroscopy/. [Accessed: Apr. 22, 2023]

[28] A. Christensen and A. Adebusuyi, “Using on-board Electrochemical Impedance Spectroscopy in Battery Management Systems,” *World Electric Vehicle Journal*, vol. 6, no. 3, pp. 793–799, Sep. 2013, doi: 10.3390/wevj6030793. [Online]. Available: https://www.mdpi.com/2032-6653/6/3/793. [Accessed: Apr. 22, 2023]

[29] O. Bohlen, *Impedance-based battery monitoring*. Shaker, 2008 [Online]. Available: http://publications.rwth-aachen.de/record/50539/files/50539.pdf

[30] R. Mingant, J. Bernard, and V. Sauvant-Moynot, “Towards Onboard Li-ion Battery State-of-health Diagnosis by a Virtual Sensor,” *World Electric Vehicle Journal*, vol. 5, no. 2, pp. 405–411, Jun. 2012, doi: 10.3390/wevj5020405. [Online]. Available: https://www.mdpi.com/2032-6653/5/2/405. [Accessed: Apr. 22, 2023]